Swiss Impulse Radiating Antenna (SWIRA) Characterization in the Presence of a Local Ground Plane (Earth)

F. M. Tesche

E_{MC} Consultant, 1519 Miller Mountain Road, Saluda, NC 28773
Department of ECE, Clemson University, Clemson, SC 29634-0915

D. V. Giri
Pro-Tech, 11-C Orchard Court, Alamo, CA 94507-1541
Department of ECE, University of New Mexico, Albuquerque, NM 87130

and

Markus Nyffeler
armasuisse, Science and Technology, HPE – Laboratory
Feuerwerkerstrasse 39, CH-3602 Thun, Switzerland

Abstract

This note characterizes the radiated EM fields from the Swiss Impulse Radiating Antenna (SWIRA). The antenna geometry is described and a computational model capable of reproducing both the prepulse and aperture radiation components from the antenna is summarized. Using this model, we then perform a study of both the transient and frequency domain spectral responses of the antenna, providing estimates of the E-field behavior at different ranges and observation angles from the antenna. The effect of the presence of a local ground plane (earth) on the radiation characteristics of the SWIRA are also evaluated in this note

Acknowledgement

Contents

1. Introduction

In the late-1990's an Impulse Radiating Antenna (IRA) was designed by D. V. Giri and constructed at the NEMP Laboratory in Spiez [1]. This type of antenna has been built or purchased by a large number of research laboratories worldwide, and its basic principles of operation have been thoroughly documented in the literature, including references [2, 3].

At the Spiez NEMP laboratory, this antenna has been in use both as a transient and CW radiator, and its application to a Swiss Civil Defense Program has been documented in several reports [4, 5]. This antenna is illustrated in Figure 1.

Figure 1.   Illustration of the old impulse radiating antenna (IRA) at the NEMP Laboratory in Spiez.

Recently, there has been an interest in upgrading the Swiss IRA to have a faster rising and larger amplitude radiated pulse from the antenna, and to provide the possibility of having both vertical and horizontal polarization of the radiated E-field. A preliminary design of these new antennas was documented in a report by Dr. Giri [6], and in the spring of 2005, work began on the construction of the two new antennas, which are referred to as the Swiss IRAs (SWIRA).

For one of these new antennas, the parabolic dish from the old IRA shown in Figure 1 was used, and for the other, another salvaged dish having the same diameter and focal length was obtained. Due to recent improvements in the feed arm design, new feed arms for each antenna were constructed. In addition, a new pulser was procured from FID Gmβh in Germany [7]. This pulser provides a sub-nanosecond voltage pulse of 10 kV applied to the antenna.

We have used the manufacturer specified pulser waveform, together with the SWIRA geometry to develop predictions of the radiated fields from the antenna for both polarizations.

This note discusses the expected radiated field environments for the new SWIRAs. In Section 2, the antenna geometry is reviewed and the pulser voltage source exciting the antenna is defined. In addition, the computational model for evaluating the E-fields radiated from this antenna in both the near field and far-field is described.

Section 3 of this note documents the use of this computational model for predicting the radiated E-fields from the SWIRA antennas. Transient and frequency domain E-fields are presented for the antenna operating in free-space and also in the presence of a lossy earth. The note concludes with a brief summary in Section 4 and references are provided in Section 5.

Appendix A of this note contains a brief validation of the computational model used for this study with an analytical representation of the fields that has been published by Russian investigators. It is noted that the Russian model has limitations in its ability to compute off-axis fields, while the present computational model does not have such a restriction.

2. SWIRA Model Development

2.1 Antenna Geometry

The SWIRAs employ a standard IRA design, as discussed in [2 and 8] and shown in Figure 2. In this antenna, there are two 400 Ω conical transmission lines that form feed-arms connecting the equivalent voltage source at the focus of the parabolic dish to the edge of the dish. Each feed arm is terminated in a resistance of 200 Ω at the dish edges (not shown in the diagram), and this provides a total of 400 Ω as a matched termination resistance at the ends of each of the two feed arm assemblies. (See ref. [6] for more details of the feed arm construction.) The only difference between the vertical and horizontally polarized SWIRA is the connection details of the voltage source at the apex of the feed structure, so that one radiates a vertical E-field, and the other radiates a horizontal field.

For the two SWIRAs, the parabolic dishes have a diameter D of 1.8 meters and a focal distance F of 0.482 meters, resulting in a F/D ratio of 0.27, which is not necessarily optimal. The total voltage exciting the feed arms across the dish is effectively double the pulser voltage V_o, due to the way that the pulser is connected to the feed arms. Details of the feeding of the IRA are provided in ref. [9].
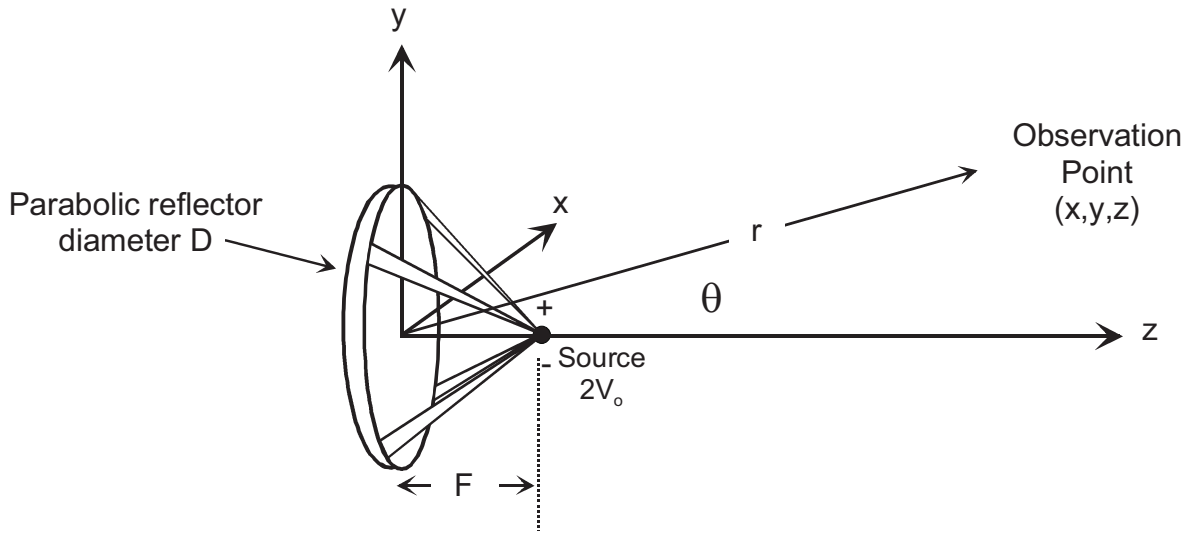

Figure 2.   Geometry of the SWIRA, showing the coordinate system and a distant field observation point.

The EM field produced by the antenna is described in the coordinate system shown in Figure 1. At observation ranges sufficiently far from the antenna, the observation point is said to be in the "far field" of the antenna. Giri [20] has shown that for an IRA of diameter D, the far-field is located in the region

$$r \geq \frac{D^2}{2c\tau_r} \tag{1}$$

where τ_r is the rise time of the pulser source exciting the antenna. For a 1.8 meter antenna and a pulser with a rise time of 140 ps, which is the nominal rise time of the FID pulser, the far-field is for $r > 38$ meters. Of course, for observation points closer than 38 meters, there is a strong transient EM field produced, but there can be radial as well as transverse field components. The EM field produced by the antenna in this range does not appear as a simple plane wave.

2.2 Antenna Excitation Source

The FID pulser is reported by the manufacturer to produce a 10 kV output pulse (into a 50 Ω load) with a wave shape as shown in Figure 3. To use this waveform for an analysis of the EM fields produced by the SWIRA, we will use a smooth, analytical fit to the overall pulse shape.
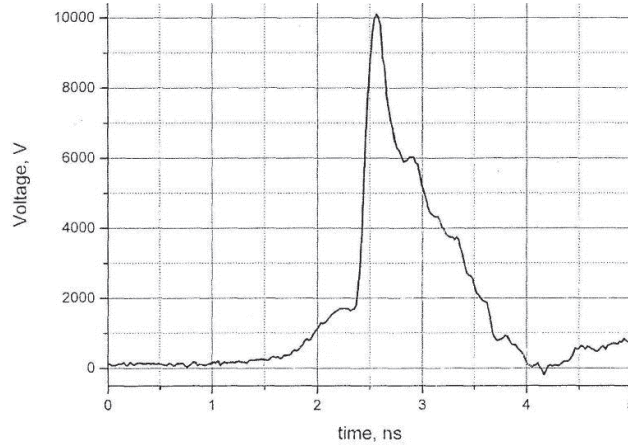

Figure 3.   The FPG 10-50MK pulser voltage waveform into a 50 Ω load.

According to Giri in ref [10], one possible representation of a pulse like that in Figure 3 is given by the expression

$$V(t) = V_0\left(1+\Gamma\right)e^{-\beta\left(\frac{t-t_s}{t_d}\right)}\left[0.5\,\mathrm{erfc}\left(-\sqrt{\pi}\,\frac{t-t_s}{t_d}\right)u\left(-(t-t_s)\right)+\left[1-0.5\,\mathrm{erfc}\left(\sqrt{\pi}\,\frac{t-t_s}{t_d}\right)\right]u\left(t-t_s\right)\right] \quad (2)$$

where *erfc*(.) denotes the complementary error function and *u*(.) is the unit step (Heaviside) function. Using this equation, it is found that the following parameters provide a reasonable fit to the pulser waveform:

$$V_O = 10,000 \text{ (V)}, \ \Gamma = 0.24, \ \beta = 0.25, \ \tau_d = 140 \text{ (ps)}, \ \tau_s = 2.4 \text{ (ns)}$$

Figure 4 presents the resulting analytical pulser waveform, as given by Eq.(2), and this waveform will be the excitation for all transient calculations in this note.
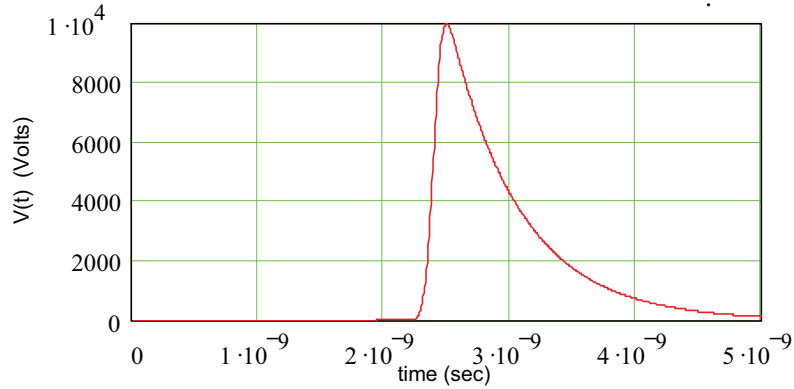
Figure 4. **Analytical representation of the pulser waveform in Figure 3, as provided by Eq.(2).**

The frequency domain spectrum of the waveform in Eq.(2) can be expressed analytically as

$$\tilde{V}(\omega) = \frac{V_0(1+\Gamma)t_d}{(\beta + j\omega t_d)} \exp\frac{1}{4\pi}(\beta + j\omega t_d)^2 \quad \text{(Volts / Hz)} . \tag{3}$$

A plot of the magnitude of this spectrum is provided in Figure 5. Note that this excitation has significant spectral components to about 5 GHz,
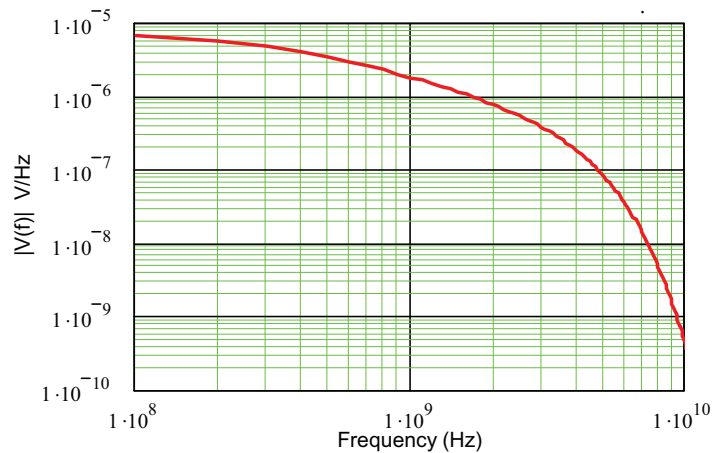

Figure 5. **Plot of the spectral magnitude of the excitation voltage waveshape of Figure 4.**

8

2.4 Determination of the Radiated EM Fields

Reference [11] has developed an analytical expression for the near- and far-field transient E-field produced by an IRA fed by a two-arm feed structure similar to that shown in Figure 6. The advantage of this analysis is that the transient E-field is given directly, without the need of Fourier transforms applied to a spectral response. In addition, the results from [11] are valid for both on-axis and off-axis observation locations, as long as the observation point lies within a cylindrical region extending from the dish edge in the boresight direction. Thus, this analysis is valid only for observation angles θ very close to zero.

To be able to compute the radiated E-field from the antenna for a wider range of observation angles, an alternate analysis is needed. One possible approach is to use a frequency domain analysis of the radiated field for a continuous wave (CW) source, and then construct the transient response using a fast Fourier transform (FFT). This is the approach that is taken in this note.
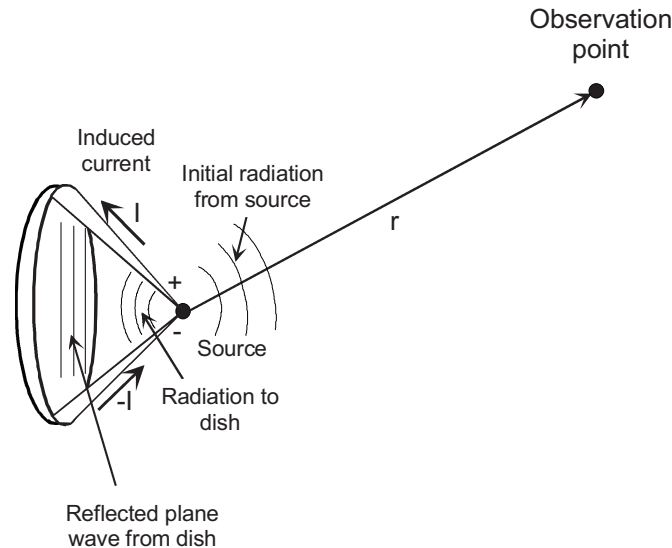

Figure 6.   Illustration of the radiation mechanisms in an IRA fed by a two-arm transmission line.

In examining the antenna structure in Figure 6 we note several contributors to the EM field radiation at a distant observation plane. At time $t = 0$ when the pulser first fires, a current traveling wave begins to flow in the transmission line feed structure from the source to the dish antenna. This current carries with it a spherical TEM field similar to the planar TEM field in a parallel two-wire transmission line. In addition, this current produces a radiated EM field in the backward direction from the source (toward the observer). This initial response seen by the observer is referred to as the "prepulse".

When the traveling current on the feed structure reaches the antenna dish, it sees a termination resistance between the feed arms and the dish (not shown in the figure). This resistance is chosen so that there is no reflection of the traveling current wave. In this case, where the feed structure is designed to have a characteristic impedance of 400 Ω, there is a 200

Ω resistance between each arm and the dish – providing a total of 400 Ω as seen by the current wave at the dish.

Thus, the current traveling wave flows onto the parabolic dish, bringing with it the TEM field that illuminates the dish. This incident EM field is reflected in the dish, and because of the parabolic shape of the dish, it re-emerges as a plane wave propagating back toward the source and then off to the observation point. This contribution to the radiation field from the antenna is a large amplitude, spike-like waveform and appears similar to an impulse function. The area under the impulse is finite (non-zero) and is equal and opposite to the area under the prepulse. The two areas together add up to zero.

2.4.1   Evaluation of the Impulse-like Radiated Field

The principal component of the radiated field from the antenna arises from the reflected TEM wave in the parabolic dish. As noted in [12], the radiated field at a distant observation point from the aperture can be expressed by three different methods:

1. By an integration of the tangential E- and H-fields in the aperture.
2. By an integration of the tangential H-field in the aperture, or
3. By an integration of the tangential E-field in the aperture.

Each of these methods is approximate and each uses a different Green's function for the integration. As noted in [12] each integration method gives the same result for on-axis fields, but the results begin to deviate from each other for large values of the observation angle θ.

For the present analysis, we elect to use the third integration method involving just the tangential E-field in the aperture. Noting the definition of the "magnetic current" $\overrightarrow{M}$ in terms of the aperture E-field as

$$\overrightarrow{M} = -2\,\hat{n}\times\overrightarrow{E}_{ap} \tag{3}$$

Balanis [13] expresses the radiated E-field in the frequency domain as integrals over the aperture equivalent magnetic currents as

$$E_x = -\frac{1}{4\pi}\iint\limits_{aperture}(z-z')M_y\frac{1+jkR}{R^3}e^{-jkR}dx'dy'$$

$$E_y = \frac{1}{4\pi}\iint\limits_{aperture}(z-z')M_x\frac{1+jkR}{R^3}e^{-jkR}dx'dy' \tag{4}$$

$$E_z = -\frac{1}{4\pi}\iint\limits_{aperture}\left[(y-y')M_x-(x-x')M_y\right]\frac{1+jkR}{R^3}e^{-jkR}dx'dy'$$

In this expression, R is the distance from an aperture integration point at location (x', y',0) to the observation point, and consequently, it varies as the integration point moves in the aperture. Note that this expression is valid both in the near, and far field.
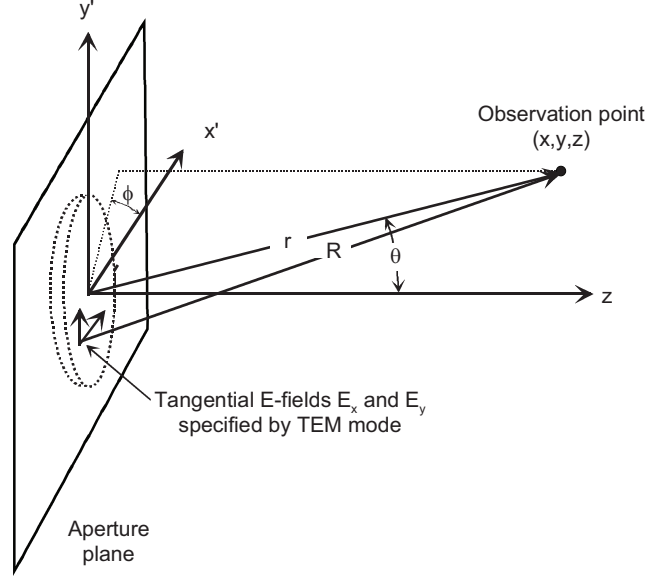
10

Figure 7.   Illustration of the integration of the tangential E-fields in the aperture to calculate the distant E-field.

The aperture excitation E-field (and hence the magnetic current $\vec{M}$ over the aperture) is assumed to be equal to the TEM mode arising from the feed arm. For a 4-arm feed structure as shown in Figure 2, ref.[14] uses a complex potential w in the aperture plane defined as

$$w(x+jy) = u(x+jy) + jv(x+jy) \qquad (5)$$

by which the E-field components can be evaluated as

$$E_x = \frac{V_o}{\Delta u} \frac{\partial u}{\partial x} \quad ; \quad E_y = -\frac{V_o}{\Delta u} \frac{\partial u}{\partial y} \qquad (6)$$

Note that the magnetic current components in Eq.(4) are given by $M_x = E_y$ and $M_y = -E_x$.

Figure 8 shows the IRA aperture and the locations of the feed arm connections and applied voltage polarities. As discussed in [14], for circular wires the complex potential for a unit-radius aperture is given by the function

$$w(x,y) = \ln\left(\frac{(x+jy)+a(1+j)/\sqrt{2}}{(x+jy)-a(1+j)/\sqrt{2}}\right) + \ln\left(\frac{(x+jy)+a(-1+j)/\sqrt{2}}{(x+jy)-a(-1+j)/\sqrt{2}}\right). \qquad (7)$$

where a = D/2 is the dish radius.

The potential function in Eq.(7) is valid for circular conductors. Reference [15] discusses alternate potential functions that can be used for the feed arms having a flat plate geometry, as shown in Figure 2. The difference in these potential functions is not too large,

however, and in the aperture model used in this study, we use the circular wire potential function of Eq.(7).
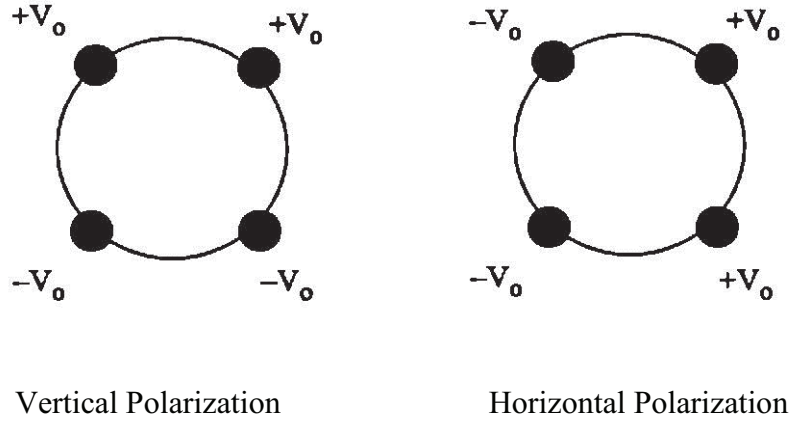

Vertical Polarization   Horizontal Polarization

Figure 8.   Diagram of the IRA aperture showing the orientation of the four feed arm connections.

To illustrate the aperture E-field for a unit-radius aperture, Figure 9 shows a contour plot of the E-field magnitude in the plane of the aperture. The aperture edge is shown by the blue circle, and only the field within this circle is used in the integrations of Eq.(4).
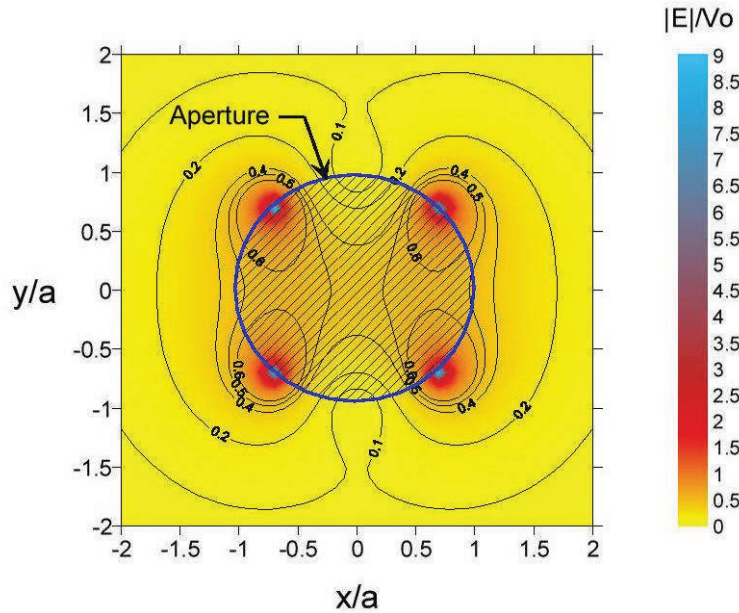

Figure 9.   Contour plot of the E-field magnitude in the plane of the aperture for a four-arm feed. The aperture edge is shown by the blue circle.

12

2.4.2 Evaluation of the Prepulse Field

As mentioned earlier, the prepulse contribution to the radiated field from the IRA is determined by including the radiation effects of the currents flowing in the feed arms. As noted in Figure 1 there are two sets of transmission lines that are in parallel and fed by the total voltage across the plate, $2V_o$. Because each feed arm pair is designed to behave like a transmission line with a 400 Ω characteristic impedance, the line shown in Figure 10 can be used for determining the spatial current distribution on the feed arms. From this current distribution, the radiated field can be determined by integrations over the spatial extent of the currents. It should be noted that these prepulse fields can also be determined using closed-form expressions developed in [15] using a stereographic projection technique.
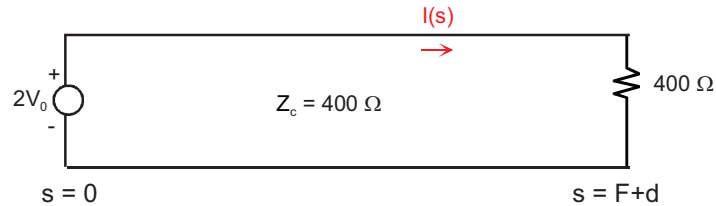

Figure 10. A matched transmission line with characteristic impedance Z_c = 400 Ω representing one of the two feed arm pairs, which are connected to the source in parallel.

In Figure 10 the parameter s denotes the distance along the feed arm, which is equal to $F+d$, where d is the distance from the dish to the aperture, as noted in the cross-section diagram in Figure 11. For this parabolic reflector, the value of d is a function of D and F and for the SWIRA dimensions is given as

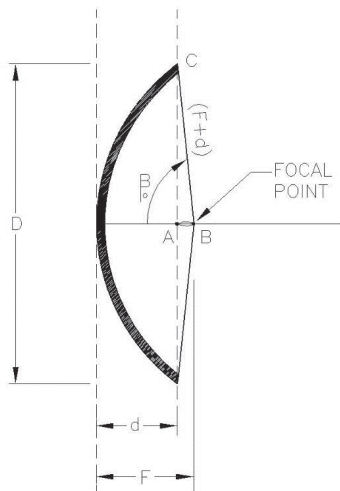$$d = \frac{D^2}{16F} = 0.42 \ m. \tag{8}$$

Figure 11.   Side view of the IRA.

13

From simple transmission line theory [12] the current along the matched transmission line is given by

$$I(s) = \frac{2V_o}{Z_c} e^{-j\omega s/c} . \tag{9}$$

Using the frequency domain expressions for the E-field produced by a point current element *Idl* located along the z-axis in Eq.(10) (see Figure 12), together with the feed arm current distribution of Eq.(9), the radiated E-field from the four current arms can be determined. This is done by mapping the E-field components in Eq.(10) into the proper IRA coordinate system by a rotation of the current source, and then summing over each of the feed arms.

$$dE_r = \frac{Idl\cos(\theta)}{2\pi} k^2 Z_o \left[\frac{1}{(kr_o)^2} - \frac{j}{(kr_o)^3} \right] e^{-jkr_o} \tag{10a}$$

$$dE_\theta = \frac{Idl\sin(\theta)}{4\pi} k^2 Z_o \left[\frac{j}{kr_o} + \frac{1}{(kr_o)^2} - \frac{j}{(kr_o)^3} \right] e^{-jkr_o} \tag{10b}$$

In this expression, $k = 2\pi f/c$ and $Z_O = 377 \ \Omega$.
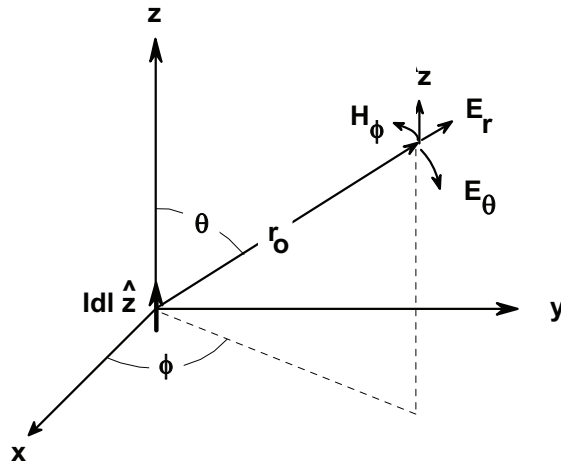

Figure 12.   Illustration of a single, z-directed current element of moment *Idl*.

Combining the aperture radiated field from Eq.(4) and the feed arm fields from Eq.(10) provides the total E-field spectrum at a particular frequency ω. This spectrum is then multiplied by the excitation spectrum of Figure 5, and by taking an inverse FFT, the transient E-field waveform from the IRA results.

The resulting on-axis transient response from the IRA computed from this frequency domain approach has been compared with the direct time domain solution of ref. [11], with very good agreement. Results of this comparison are presented in Appendix A.

14

2.5 Effects of the Earth on the SWIRA Radiation

In the discussion of the EM fields produced by the SWIRA in the previous sections, the effects of a nearby earth have been neglected. In most operational scenarios for the SWIRA, however, there will be an imperfectly conducting earth in the vicinity of the antenna, and as shown in Figure 13 this will modify the EM field at a distant observation point. Shown in this figure is a direct wave contribution radiating from the antenna and propagating to the distant observer over a path R_1. In addition, there is a wave leaving the antenna at a different angle, reflecting off of the ground, and then propagating to the observation point on path R_2. In addition to these "space waves", there is a surface wave on the earth, as discussed further below. Thus, the total field consists of the sum of these three wave components, and it is a complicated function of the antenna and observer heights h_1 and h_2, the distance d, the earth parameters σ and ε_r, and the directional radiation characteristics of the SWIRA. The analysis of this SWIRA configuration is described in this section, which is derived from ref. [16].
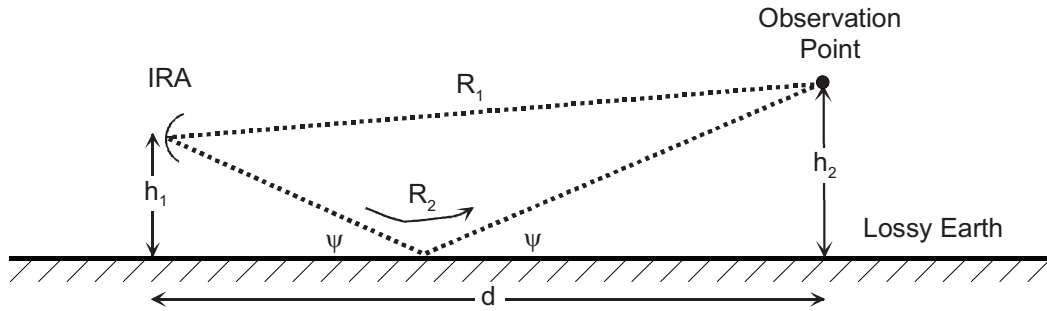

Figure 13.   Illustration of the IRA located over a lossy earth.

From Snell's law, the angle of incidence is equal to the angle of reflection, and this can be expressed from the geometry of Figure 13 as

$$\psi = \tan^{-1}\left(\frac{h_1 + h_2}{d}\right). \tag{11}$$

where the two distances R_2 and R_1 are given as

$$R_2 = d\left[\left(\frac{h_1 + h_2}{d}\right)^2 + 1\right]^{1/2} \quad and \quad R_1 = d\left[\left(\frac{h_1 - h_2}{d}\right)^2 + 1\right]^{1/2}. \tag{12}$$

In examining Figure 13 it is apparent that the earth-reflected field will arrive at the observer at a time slightly later than the direct signal from the antenna (along path R_1). This differential time is expressed as

$$\Delta t = \frac{R_2 - R_1}{c}, \tag{13}$$

15

and a plot of this time difference is provided in Figure 14 as a function of range d for the specific case of $h_1 = h_2 = 1.5$ m.
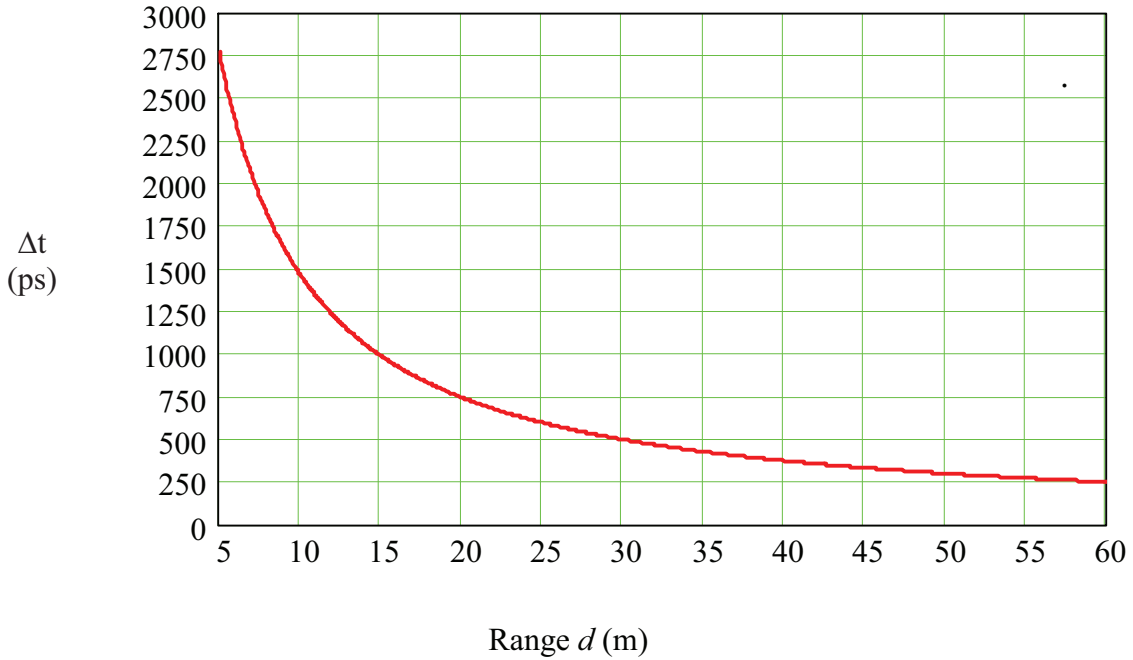

Figure 14.   Plot of the time difference in arrival of the earth-reflected pulse relative to the direct pulse.

This arrival time information helps to understand the behavior of the fields to be presented in Sections 3.2 and 3.3, but it does not tell the complete story, as the strength of the earth-reflected field is modified by the electrical properties of the earth. Moreover, as discussed in [12] there can be a surface wave contribution to the field in addition to the direct and reflected waves.

A simple but useful expression for the total E-field of the IRA in the presence of the earth is given by Eq.(14), which is provided by Angelakos [17]. A more complete theory of antenna radiation in the presence of the earth described by Jordan and Balmain [18], and their expressions for the earth effects on the radiated EM fields have been applied to the study or radiation from the ARES EMP simulator by Tesche, et. al. [19].

In this simple model, the total E-field at the observation point is represented as a sum of the direct, reflected and surface wave components as

$$\frac{E}{E_o} \cong 1 \quad + R\, e^{-j\Delta\phi} \quad + \quad (1-R)\, A\, e^{-j\Delta\phi} \tag{14}$$

where R is the Fresnel reflection coefficient for vertical or horizontal polarization given in [12, 18] as

16

$$R_v(\Psi, f) = \dfrac{\varepsilon_r\left(1+\dfrac{\sigma}{j\omega\varepsilon}\right)\sin\Psi - \left[\varepsilon_r\left(1+\dfrac{\sigma}{j\omega\varepsilon}\right)-\cos^2\Psi\right]^{1/2}}{\varepsilon_r\left(1+\dfrac{\sigma}{j\omega\varepsilon}\right)\sin\Psi + \left[\varepsilon_r\left(1+\dfrac{\sigma}{j\omega\varepsilon}\right)-\cos^2\Psi\right]^{1/2}}, \tag{15a}$$

for the case of vertical polarization, and

$$R_h = \dfrac{\sin\psi_2 - \sqrt{\varepsilon_r\left(1+\dfrac{\sigma}{j\omega\varepsilon_r\varepsilon_o}\right)-\cos^2\psi_2}}{\sin\psi_2 + \sqrt{\varepsilon_r\left(1+\dfrac{\sigma}{j\omega\varepsilon_r\varepsilon_o}\right)-\cos^2\psi_2}} \tag{15b}$$

for the horizontally polarized case. In these expressions, ω is the angular frequency $\omega = 2\pi f$, and σ and ε_r, are the earth's electrical parameters.

As noted in [12], the surface wave contribution (the third term in Eq.(14)) for vertically polarized and horizontally polarized waves are slightly different, so that there are different attenuation functions A for vertical and horizontal polarizations. This attenuation function has the general form

$$A(v) = \left[1 - j\sqrt{v\pi}\, e^{-v} erfc\left(j\sqrt{v}\right)\right] \tag{16}$$

where the parameter v is given by

$$v = -j\frac{\omega}{c} z u^2 \frac{1-u^2\cos^2(\psi)}{2}\left[1+\frac{\sin(\psi)}{u\sqrt{1-u^2\cos^2(\psi)}}\right]^2 \quad \text{(vertical pol.)} \tag{17a}$$

$$v = -j\frac{\omega}{c} z u^2 \frac{\left(1-u^2\cos^2(\psi)\right)}{2}\left[1+\frac{u\sin(\psi)}{\sqrt{1-u^2\cos^2(\psi)}}\right]^2 \quad \text{(horizontal pol.).} \tag{17b}$$

In these last equations, ω is the angular frequency, c is the speed of light, z is the range of the observation point from the antenna, and ψ is the angle of incidence of the reflected wave on the earth (as shown in Figure 13). The term u contains information about the lossy earth, and is given as

$$u = \sqrt{\frac{1}{\varepsilon_r - j\left(\sigma/(\omega\varepsilon_o)\right)}}. \tag{18}$$

17

The value of ν for the special case of $\psi = 0$ is often referred to as the "numerical distance" p, as

$$p = |p|e^{jb} = \nu\big|_{\psi=0} \, .$$ (19)

Reference [18] provides several approximations to this numerical distance, but it is just as convenient to evaluate Eqs(17a and b) directly.

For the case of $\psi = 0$, Figure 15 plots the surface wave attenuation factor A as a function of the magnitude $|p|$ and phase angle b of the numerical distance. The angle $\psi = 0$ implies that both the source and observation points are close to the earth surface.
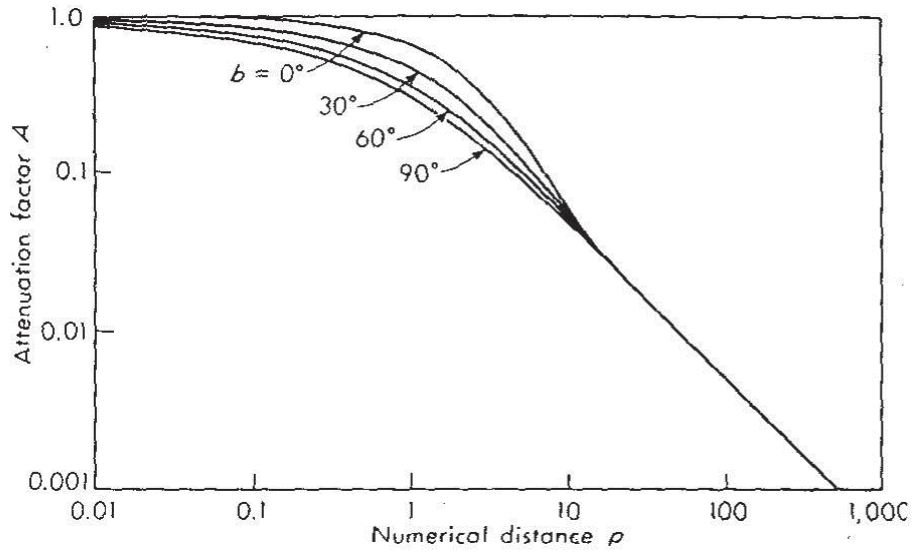
Figure 15. Plot of the surface wave attenuation function A, as a function of the parameters $|\rho|$ and b. (From ref.[18].)

The phase factor $\Delta\phi$ term in Eq.(14) is expressed in terms of the path differences as

$$\Delta\phi = \frac{\omega}{c}(R_2 - R_1) = \frac{\omega d}{c}\left\{ \left[\left(\frac{h_1+h_2}{d}\right)^2 + 1\right]^{1/2} - \left[\left(\frac{h_1-h_2}{d}\right)^2 + 1\right]^{1/2} \right\}$$ (20)

To include the effect of the earth on the IRA field, the aperture integration model described in Section 2.3 is used to compute the direct and reflected waves at an observation point (see Figure 13), assuming a perfectly conducting earth. The appropriate reflection coefficient (vertical or horizontal) is used to multiply the reflected term, as indicated in Eq.(14). The approximate surface wave term is then added and the total E-field is calculated. This calculation, of course, is conducted in the frequency domain, with the transient response being calculated by Fourier transform techniques.

18

3. Computed Responses for the SWIRA

Using the frequency domain aperture and feed structure integration model discussed in Section 2, calculations of the radiated E-field from the two SWIRAs have been performed. Recalling that the antenna diameter is $D = 1.8$ m and the focal length is $F = 0.482$ m, the antenna model provides the vector E-field at any observation point, either in the near field or far field. In the present analysis, we concentrate only on the principal E-field component. That is to say, if the antenna is fed so that the source produces a predominately E_y field (as shown in Figure 2), we will calculate the E_y field at the observation point. Clearly, by rotating the feed configuration so as to produce a horizontal E-field (E_x) excitation, the resulting radiation pattern will also be rotated. Thus, for the SWIRA antenna operating in free space, only one polarization need be considered. In this study, we will concentrate on the vertical polarization case. These responses are discussed in Section 3.1.

Also considered in this section is the case of the antenna operating in the presence of a lossy earth. As mentioned in Section 2.5, the total E-field at an observation point consists of a direct wave, an earth-reflected wave, and a surface wave. The reflected field intensity depends on the polarization of the incident field, and consequently, there is a difference between the vertical and horizontal polarization cases. Results for these cases will be discussed in Sections 3.2 and 3.3.

In all cases, the calculations are performed in the frequency domain, with the transient responses being calculated using a numerical Fourier transform. The excitation source for the SWIRA is assumed to be the analytical representation of the FID pulser, given by Eq.(2).

3.1 Isolated SWIRA

3.1.1 Transient Responses

The usual characterization of an IRA is by examining the behavior of the transient responses, either in the boresight direction of the antenna, or at other locations away from boresight. As mentioned earlier, the Russian analysis in [11] was restricted in the range of possible observation angles, so that only a limited view of the radiation field was possible. The present analysis is not limited in this manner, and consequently, a wide range of observation angles is possible. In this section, both on-axis and off-axis E-field predictions are described.

3.1.1.1 On-Axis Responses

Figure 16 shows the SWIRA geometry for the calculation of the on-axis radiated E-field. For the antenna feed with polarity as noted in Figure 2, the principal E-field component at the observation location $(x,y,z) = (0,0,z)$ is also y-directed.
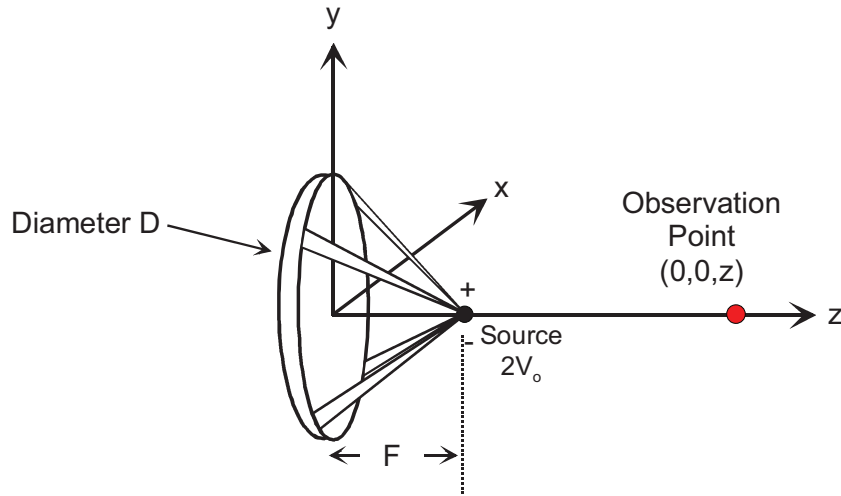
Figure 16.   Geometry for on-axis E-field responses for different values of distance *z*.

Figure 17 shows the principal radiated transient E-field from the SWIRA for different ranges *z*, ranging from *z* = 1 m to *z* = 1000 m. Shown in this figure is the prepulse contribution to the radiated field occurring at about *t* = 2.5 ns, along with the impulse-like component at about *t* = 5.5 ns. The time difference between these two waveform components is 3 ns ≈ 2*F*/*c* (*F* = 0.48 m, *c* = 3 x 10^8 m/s).
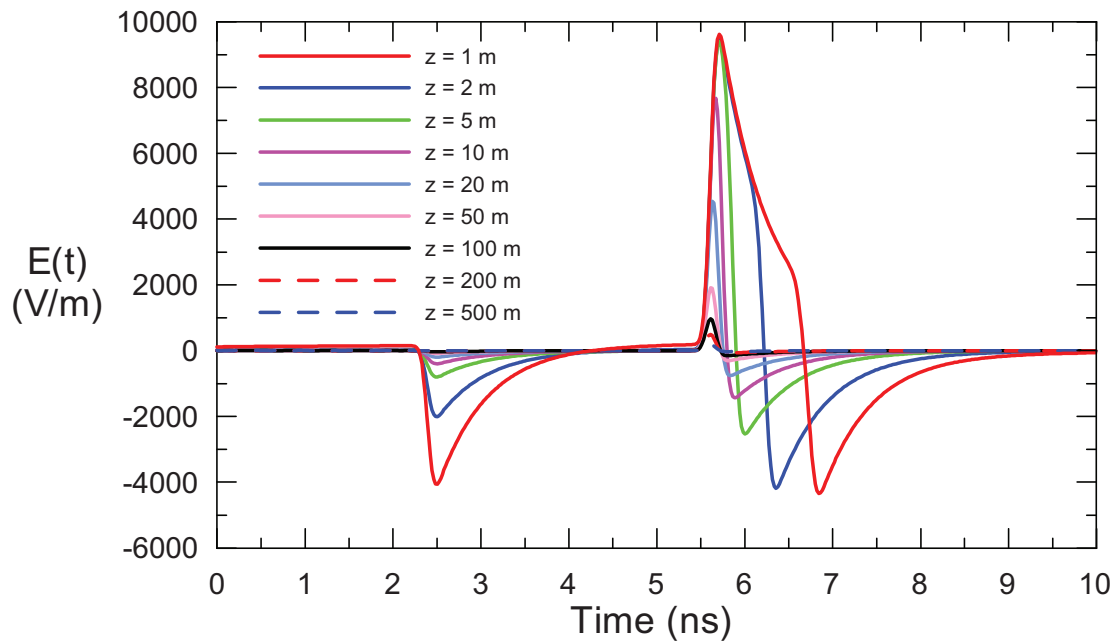
Figure 17.   Principal on-axis transient E-field produced by the SWIRA for different ranges *z*.

In ref [20] there are closed form and simple expressions for the peak prepulse and peak impulsive waveform amplitudes. For the peak prepulse we have (from Eq. 5.38 of [20])

$$E_{peak} \approx \frac{2V_o}{z} \frac{D}{4\pi f_g} \frac{1}{2F} \sqrt{2} \quad \text{(V/m)} \tag{21}$$

and for the peak impulse (from Eq. 5.39 of [20]) we have

$$E_{peak} \approx \frac{1}{z} \frac{D}{4\pi c f_g} 2 \left. \frac{\partial V_o}{\partial t} \right|_{peak} \sqrt{2} \quad \text{(V/m)}. \tag{22}$$

In these expressions, $2V_o$ is the peak voltage applied across the IRA dish (twice the peak pulser voltage, due to the voltage doubling effect of the balun), $\partial V/\partial t |_{peak}$ is the peak rate of rise of the pulser source voltage, z is the distance between the IRA and the field observation point, D is the reflector diameter, F is the focal length of the reflector and f_g is the ratio of the transmission line impedance and the free space impedance

$$f_g = \frac{Z_c}{Z_o} = \frac{400}{377} = 1.06 \quad . \tag{23}$$

Applying Eq.(21) to the particular SWIRA geometry for a near-field position of $z = 1$ meter yields a prepulse amplitude of 3980 V/m, while the present aperture/feed arm integration procedure for the same case provides a prepulse of 4058 V/m – about 2% different. Similarly, in the far field at a distance of $z = 50$ m, Eq.(22) provides a peak impulse E-field of 1820 V/m, while the present analysis yields 1916 V/m. This amounts to about a 5 % difference[1].

For observation locations close to the antenna, the peak value of the E-field is seen to be approximately 10 kV/m and this remains nearly constant over the range $1 \leq z \leq 10$ m. For an observation location greater than about 10 m, we note that both the prepulse and impulse decrease in amplitude as a function of range[2]. Figure 18 summarizes the peak value of the on-axis E-field from the SWIRA as s function of range, z, and it is noted in this plot that the field falls as $1/z$ for $z > 10$ m.

---

[1] It is noted that these calculations use an idealized rate of rise of the pulser voltage, dV/dt., which is estimated from the pulser wave shape as applied to a 50 Ω load. In the physical SWIRA, the fast rising pulser waveform is applied to the Balun, and the rise time of the output voltage that is ultimately applied across the IRA reflector is degraded. Consequently, it is estimated that the actual SWIRA peak E-field levels could be about 50% of those calculated here with the unperturbed pulser risetime.

[2] It is worth noting that the prepulse amplitude decreases at $(1/z)$ from the start, whereas the impulse-like contribution has a $(1/z)$ behavior only in the far field $(z > [D^2 / (2ct_r)])$
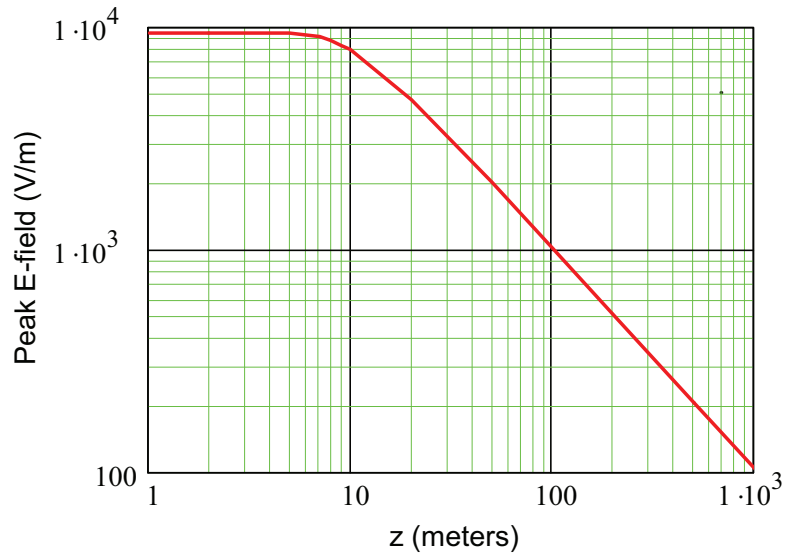
a, Un-normalized E-field
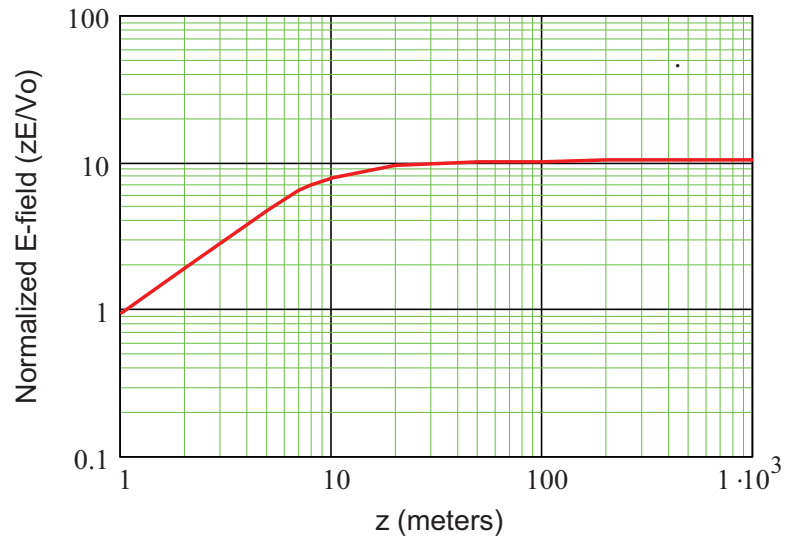
b. Normalized E-field

Figure 18.   Plots of the un-normalized (E) and normalized (zE/V_o) peak value of the on-axis E-field from the SWIRA as a function of range, z.

22

It is useful to also consider plotting the radiated on-axis transient E-field in a normalized form, given as $zE(t)/V_o$, where V_o is the peak amplitude of the pulser excitation waveform. This plot is shown in Figure 19 for the entire waveform, and in Figure 20 for just the impulse-like waveform contribution.
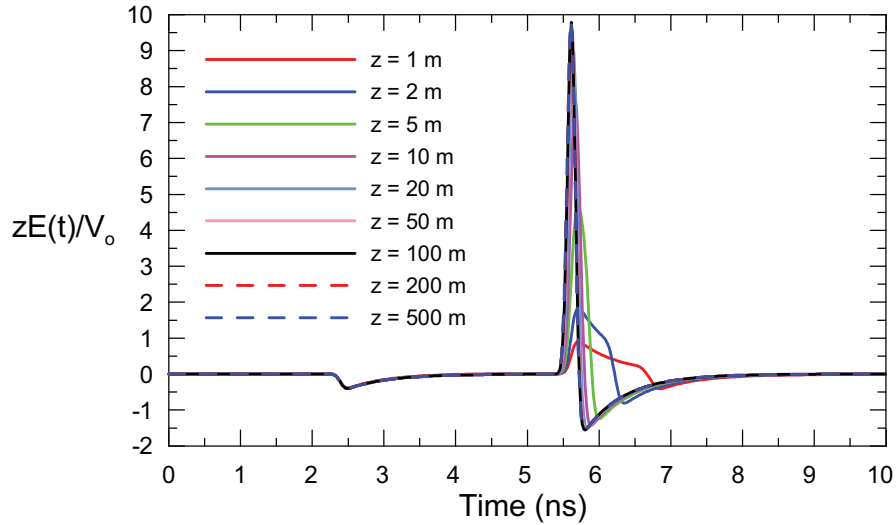
Figure 19. **Plot of the normalized on-axis transient E-field ($zE(t)/V_o$) produced by the SWIRA for different ranges, z.**
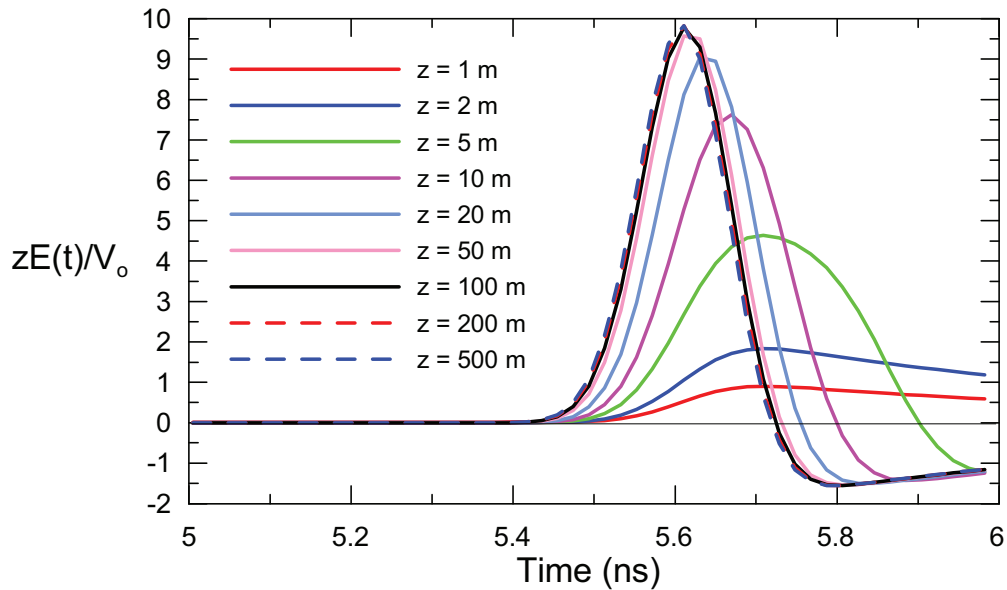
Figure 20. **Plot of the impulse-like component of the normalized on-axis transient E-field ($zE(t)/V_o$) produced by the SWIRA for different ranges, z.**

23

From these last two figures, it is clear that a single waveform for the normalized E-field $(zE(t)/V_o)$ can be used for observation locations $z > 50$ meters. These locations correspond roughly to the "far field", as given in Eq.(1), which predicts $z \geq 38$ m for the far field.

3.1.1.2 Off-Axis Response

We note that in the boresight direction, the radiated E-field has a large peak, which is similar to an impulse function. It is interesting to evaluate the behavior of this peak in an observation plane parallel to the x-y axes, as shown in Figure 21. Figure 22 presents plots of the normalized transient E-field waveforms $(zE(t)/V_o)$ in the far-field at a distance z = 500 m in a horizontal cut (part a) and a vertical cut (part b). Note that away from the boresight, the waveform begins to deviate from an impulse-like pulse; the "impulse" becomes smaller and wider as one moves off axis.
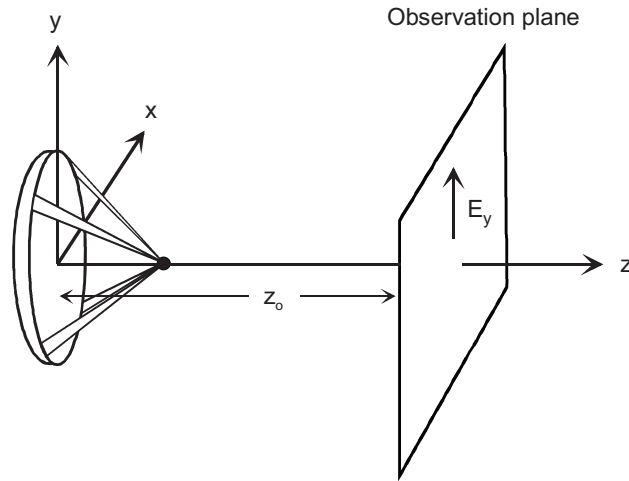
Figure 21. Illustration of the principal E_y field component observation plane at a distance of z from the IRA.
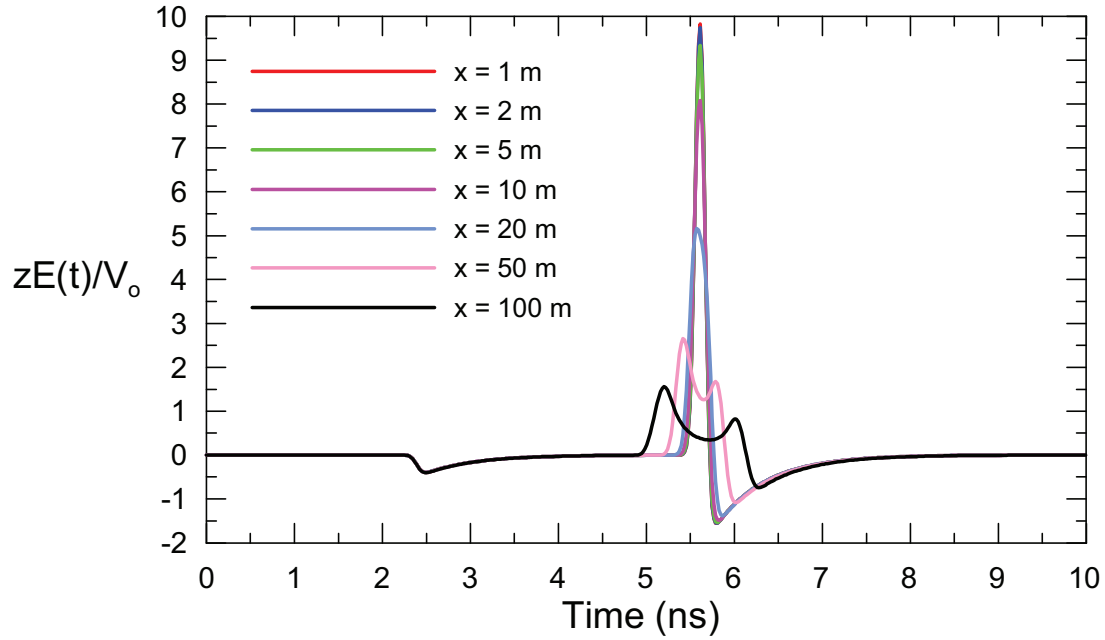
a. Plots for $y = 0$ and various x (horizontal cut)
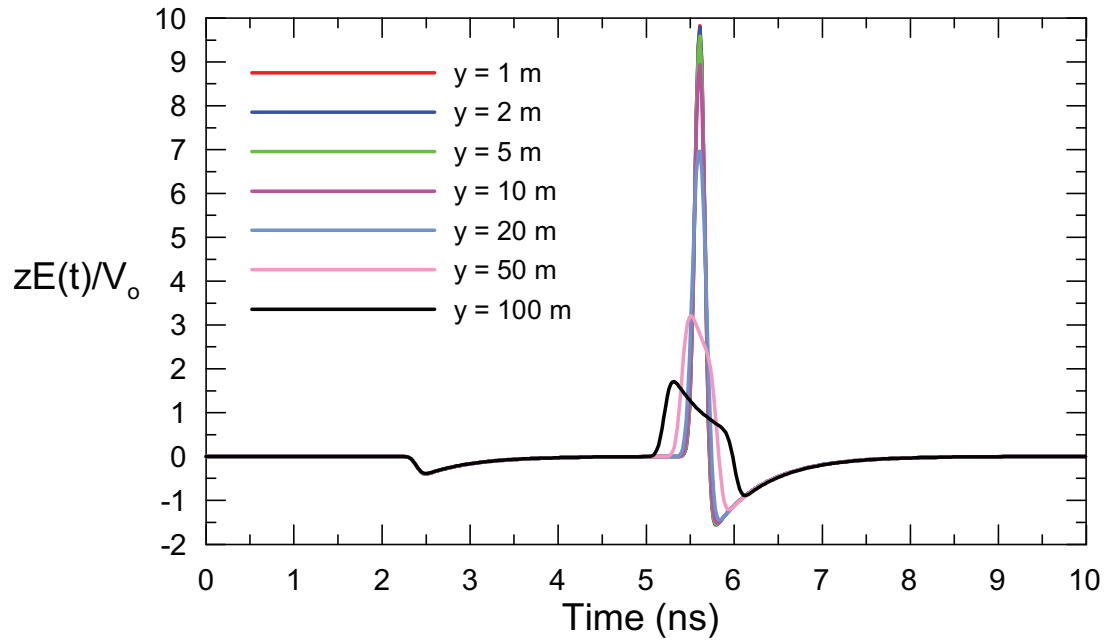
b. Plots for $x = 0$ and various y (vertical cut)

Figure 22.   Plot of the normalized transient E-field waveform in the far-field ($zE(t)/V_o$) in the plane at z = 500 m in a horizontal cut (a) and a vertical cut (b).

Figure 23 illustrates the behavior of the peak transient E-field (in V/m) in the observation plane of Figure 21 for different ranges z. In this plot, the angles subtended by the observation (with respect to the maximum x and y dimensions) are held constant to $\pm 10^o$, This plot shows that within this narrow cone-like volume, the E-field pattern lacks definition near the antenna, at ranges of 1 to 2 meters, Father away, however, in the range of 5 to 20 meters, the transient E-field peak becomes more focused to an intense, narrow beam. For ranges greater than about 50 meters, this peak amplitude pattern remains stable. except, of course, for the $1/z$ fall-off of the E-field peak amplitude.
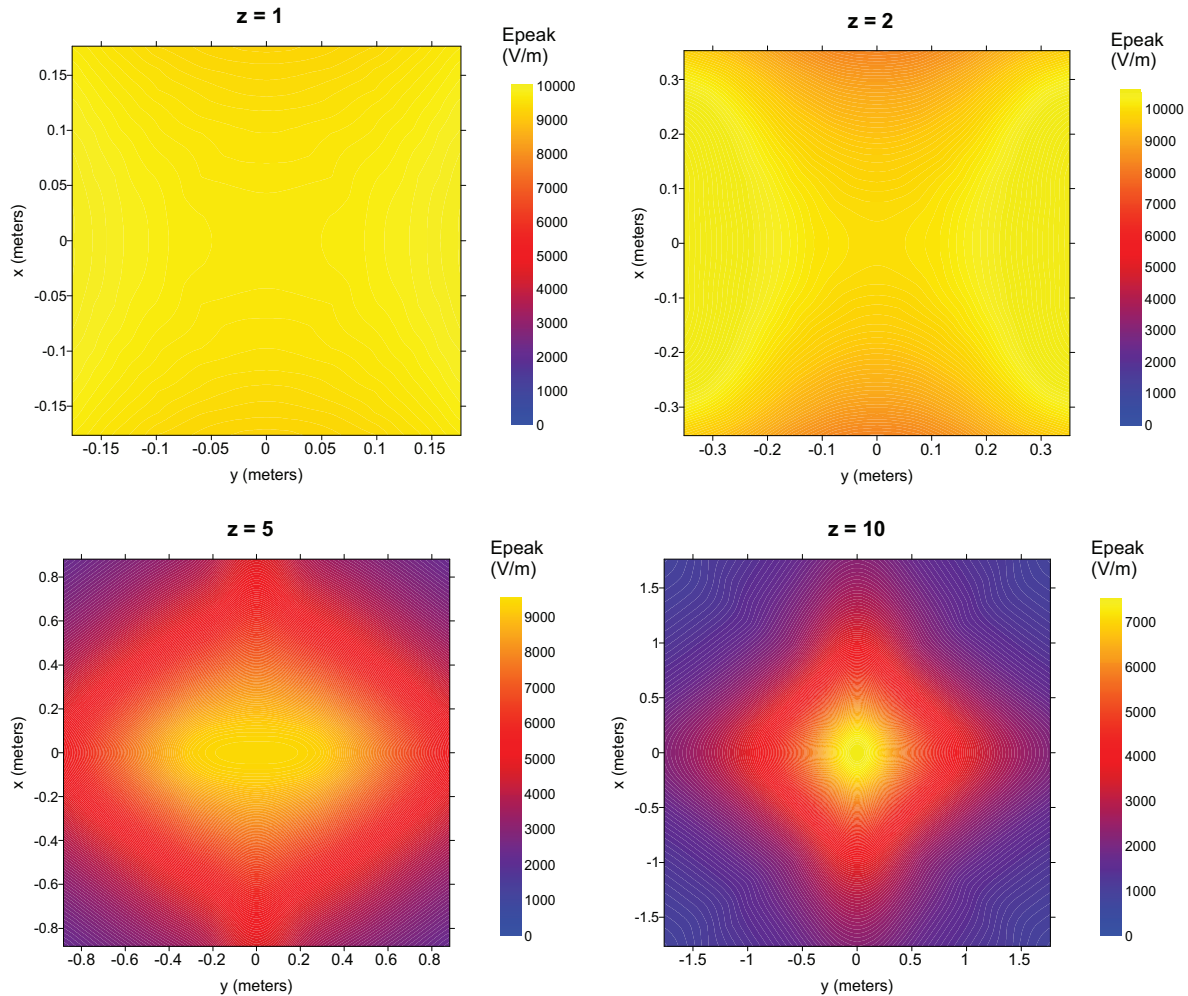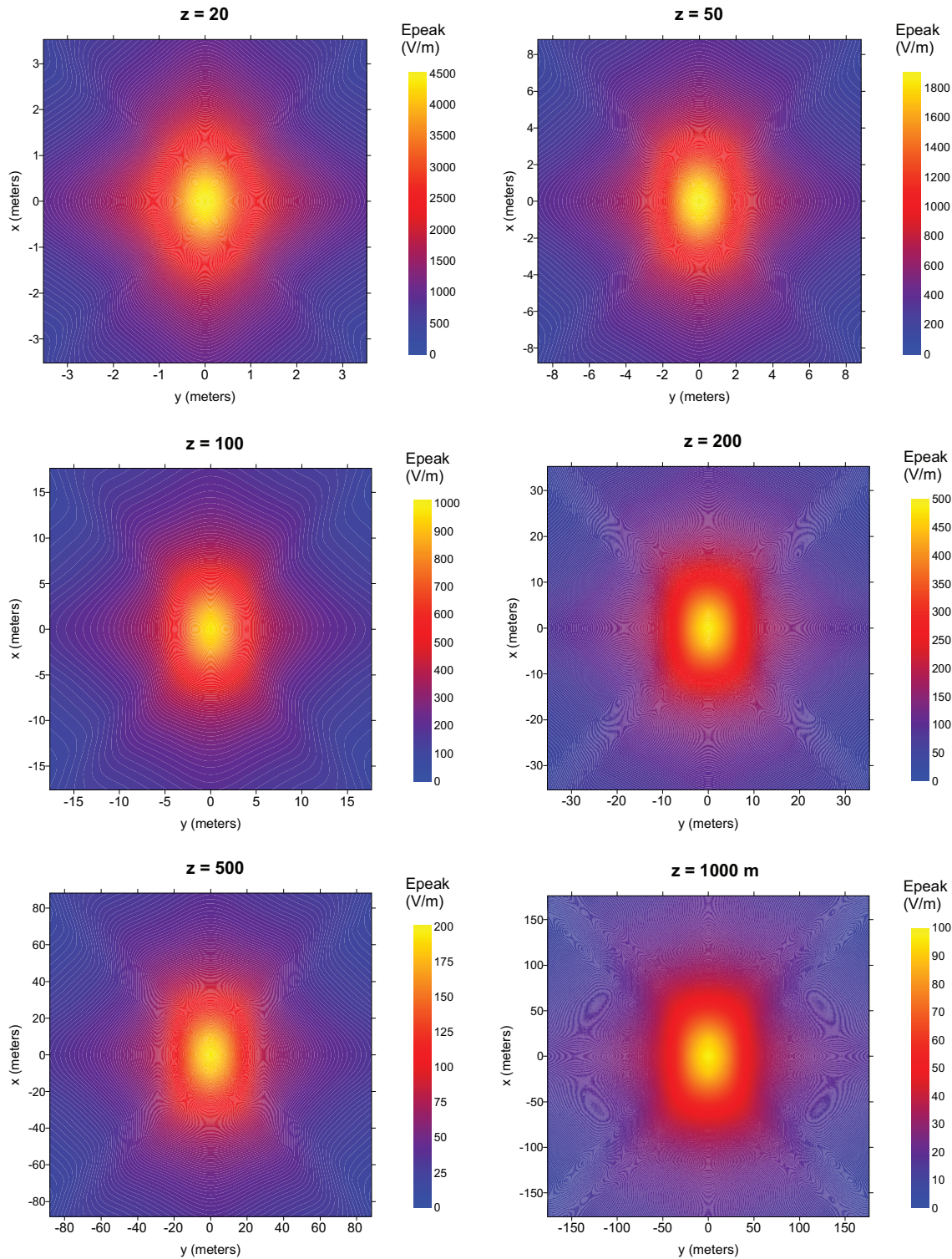
Figure 23. Color contour plots of the peak transient E-field (in V/m) in the observation plane of Figure 21 that subtends a constant angle of ± 10º in the x and y direction, for different ranges *z*.

Figure 24 presents a different way of displaying the peak transient from the SWIRA as a function of range. In this figure, the observation plane Figure 21 is maintained fixed with a size of 40m x 40 m. This represents a fixed size target at different ranges (say a large aircraft). This plot shows that near the antenna, the transient E-field is very large in a circular disk the size of the dish ($D = 1.8$ m). Consequently, in the 40m x 40m observation plane, only a very small portion of the plane is illuminated. As the range z increases, the beam broadens spatially and illuminates more of the target, with the expected 1/z fall off of the peak E-field intensity.
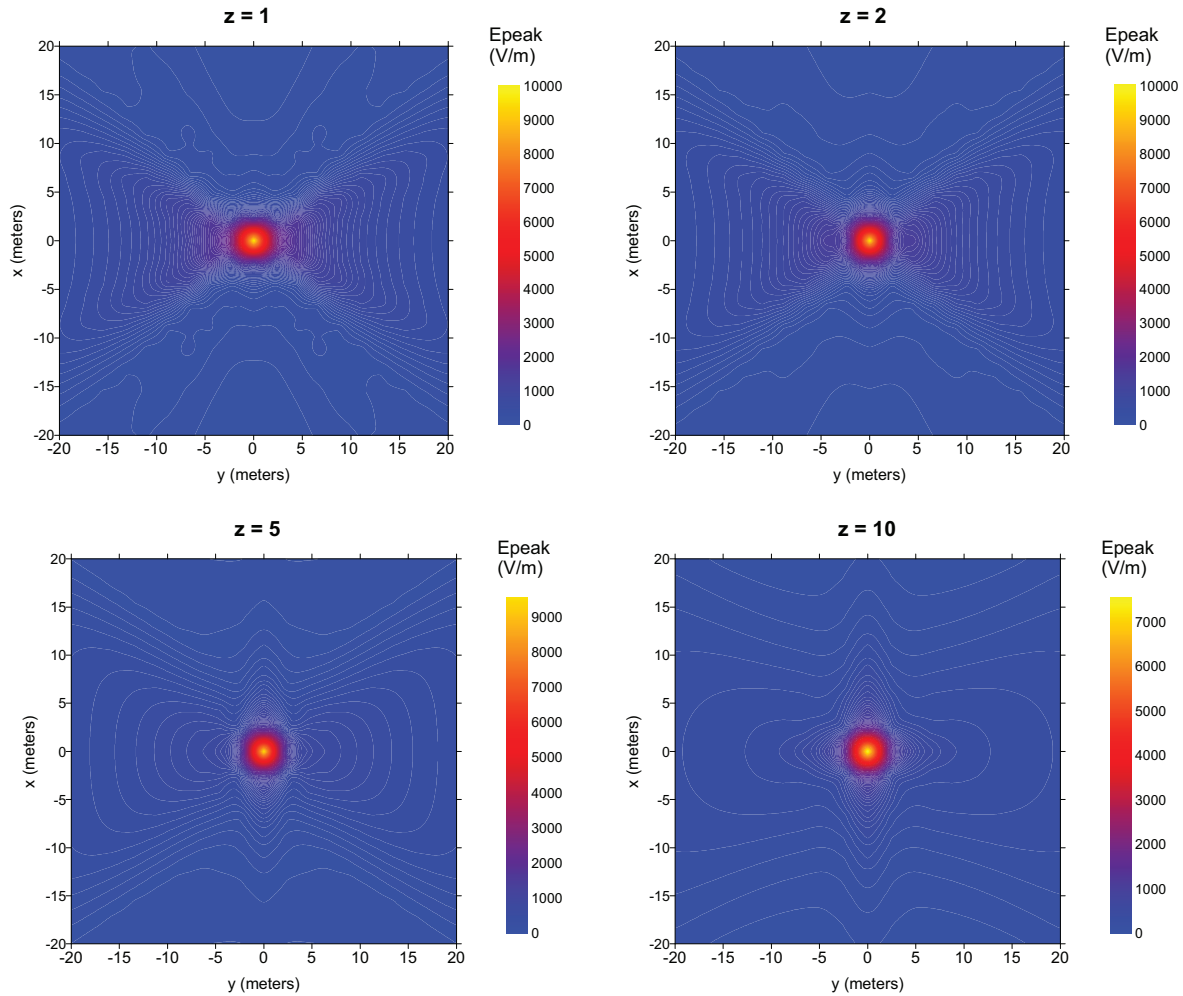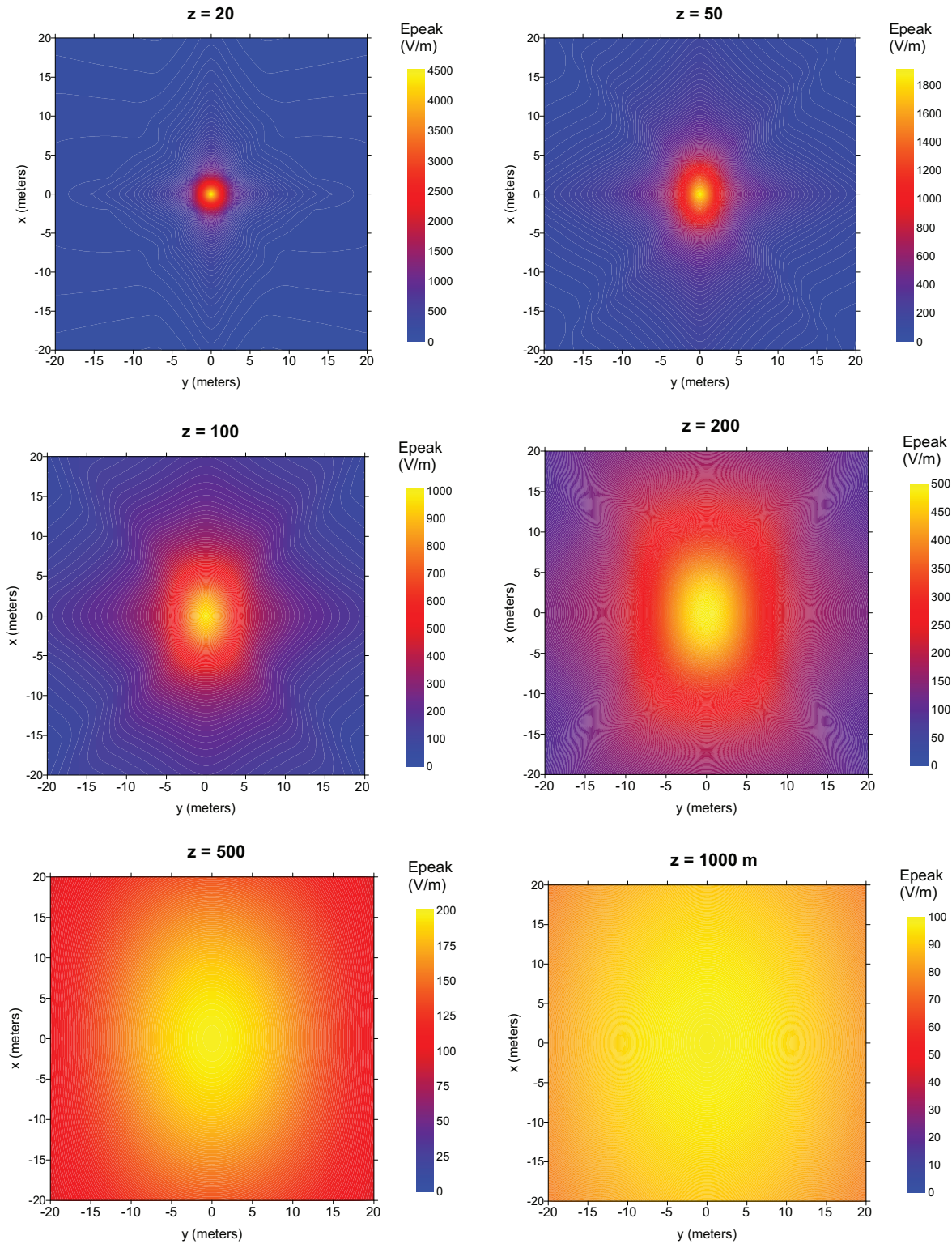
Figure 24. Color contour plots of the peak transient E-field (in V/m) in a 20m x 20 m observation plane of Figure 21 for different ranges *z*.

3.1.2 Spectral Responses

It is also instructive to examine the behavior of the SWIRAs in the frequency domain, as these antennas can also be used for CW testing [5]. This section describes the spectral responses of the antennas.

3.1.2.1 On-Axis Responses

To illustrate the spectral response of the SWIRA, Figure 25 presents the spectral magnitude of the on-axis transient E-field for different ranges, z. Notice that these spectra contain the effects of the pulser spectrum of Figure 5 and consequently, the spectra begin to roll-off for frequencies over 3 GHz.

In addition, for frequencies lower than about 200 MHz, the spectra are also rolling-off. As noted by Giri [20], this is due to limitations of the antenna aperture radiation process, which occurs when the aperture diameter is on the order of a wavelength.

The deep null at ~ 900 MHz for $z = 1$ m is observed to be the reciprocal of the differential time of the reflector edge ray and the direct ray at the observer. This is referred to at the "clear time" of the antenna [20] and it decreases with increasing z, In other words, this notch frequency increases with z and becomes inconsequential in the far field. This is more evident in Figure 26.
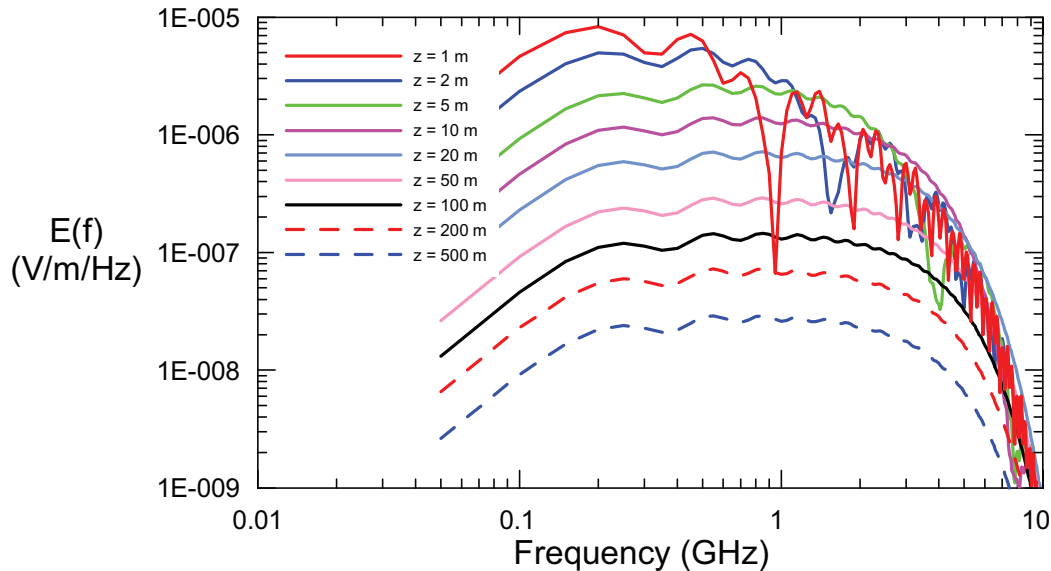

Figure 25.   Plot of the spectral magnitude of the on-axis E-field of Figure 16 for different ranges, *z*.

An alternate view of this radiated E-field spectrum is provided by examining the normalized spectrum $(zE(\omega)/V(\omega))$. This quantity is essentially a transfer function, relating the radiated field to the pulser voltage spectrum. Figure 26 presents these spectral magnitudes, and it is evident that in the far field, the radiation from the antenna is proportional to the frequency, *f*.
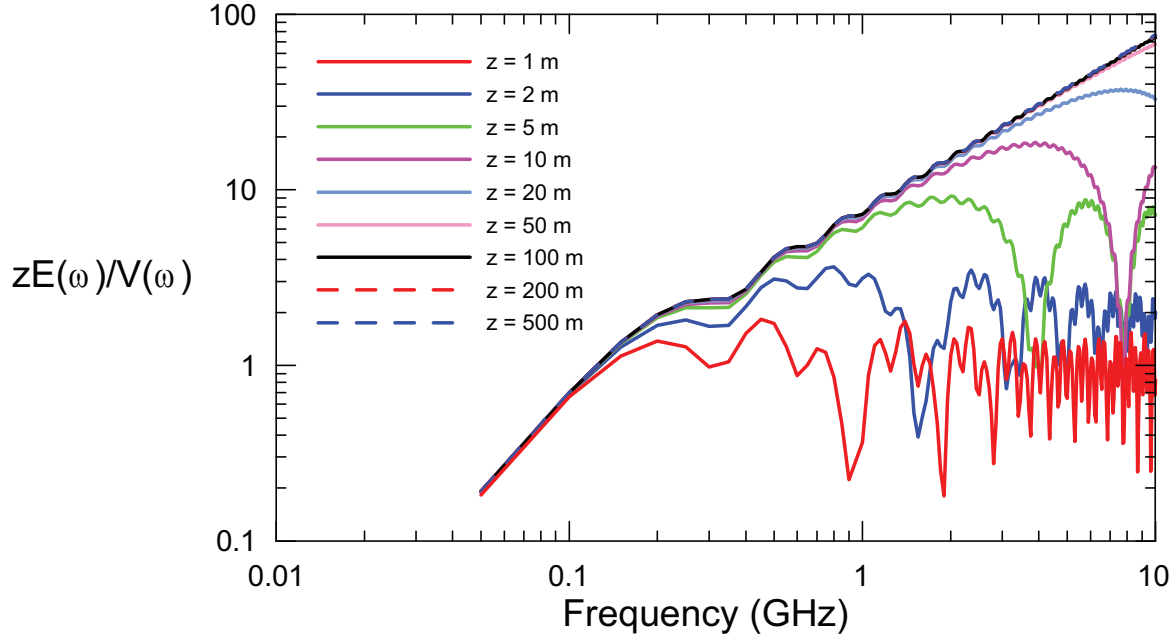
Figure 26. **Plot of the spectral magnitude of the normalized on-axis E-field ($zE(\omega)/V(\omega)$) of Figure 16 for different ranges, z.**

3.1.2.2 Off-Axis Responses

The off-axis behavior of the frequency domain spectral magnitudes in the observation plane of Figure 21 is also of interest. Figure 27 presents colored contour plots of the normalized far-field magnitude $|zE(\omega)/V(\omega)|$ for frequencies varying from 100 MHz to 5 GHz. It is noted that at low frequencies, the radiation pattern is broad, and as the frequency increases, it narrows down to a thin beam.

The normalized plots of Figure 27 are in the far-field and consequently, the value of z is not important for the data. However, this is not true in the near field. Figure 28 shows contour plots of the normalized near-field magnitude ($zE(\omega)/V(\omega)$) (at z= 5 m) for the same set of frequencies. These plots are different from those in Figure 27, principally due to the near-field static and quasi-static field components found in the expressions for the fields.

Increasing the frequency to 10 GHz and considering an observation plane only 4 meters square provides the contour plot shown in Figure 29. This plot is essentially an image of the near-field distribution and shows the "hot spots" of the antenna feed structure.
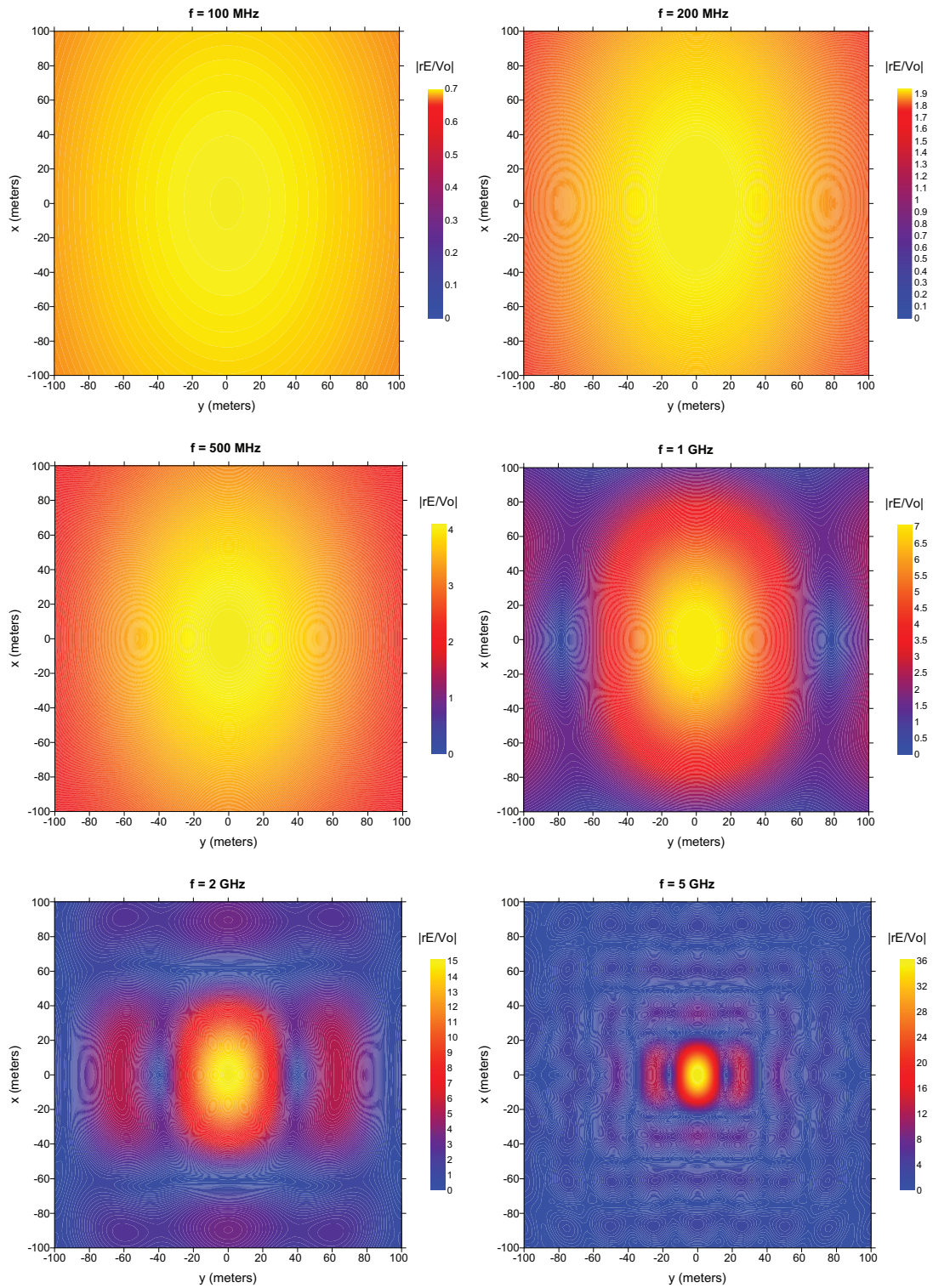
31

Figure 27. Contour plots of the normalized far-field magnitude $|zE(\omega)/V(\omega)|$ for different frequencies.
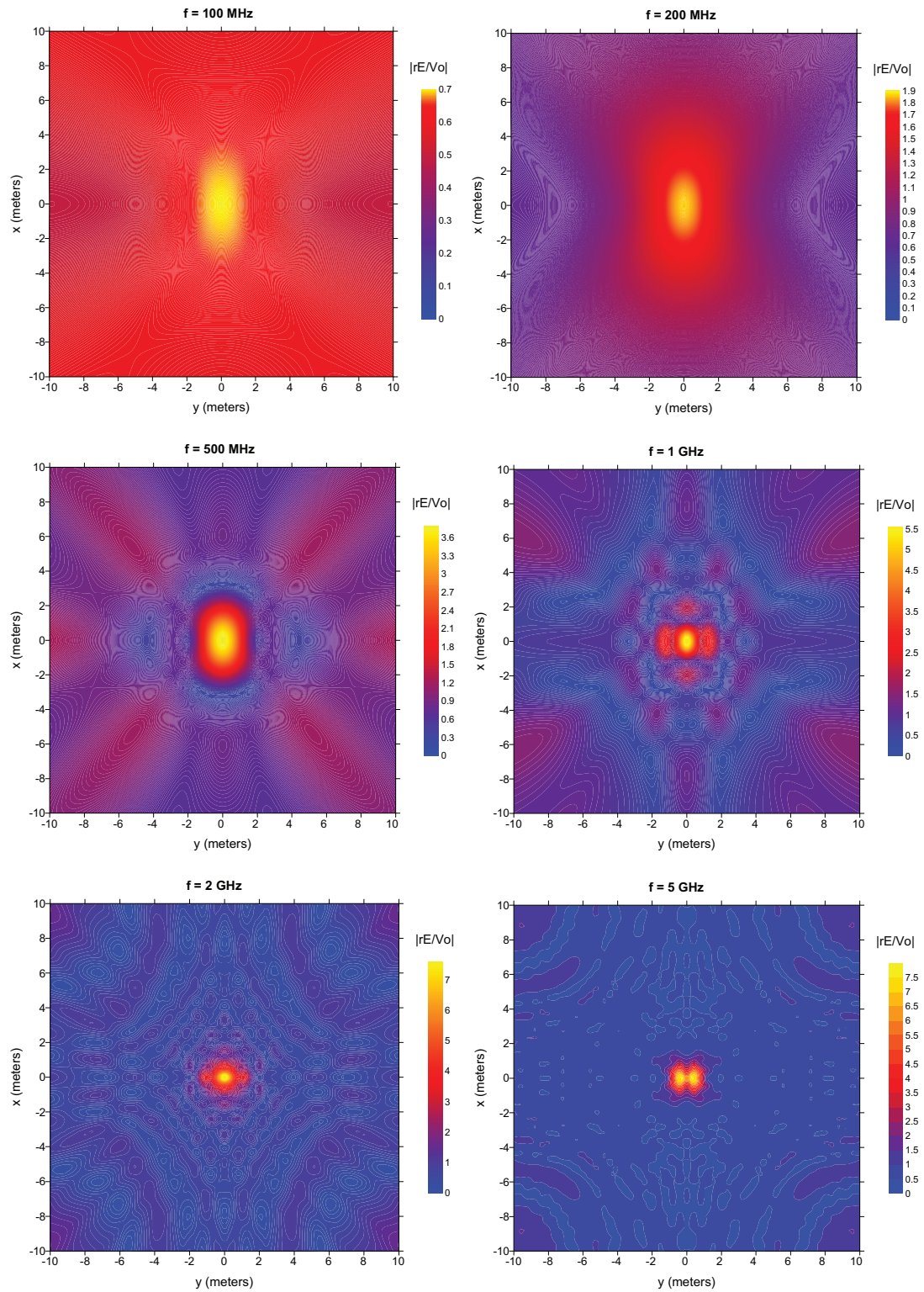
Figure 28. Contour plots of the normalized near-field magnitude ($zE(\omega)/V(\omega)$) (at $z = 5$ m) for different frequencies.
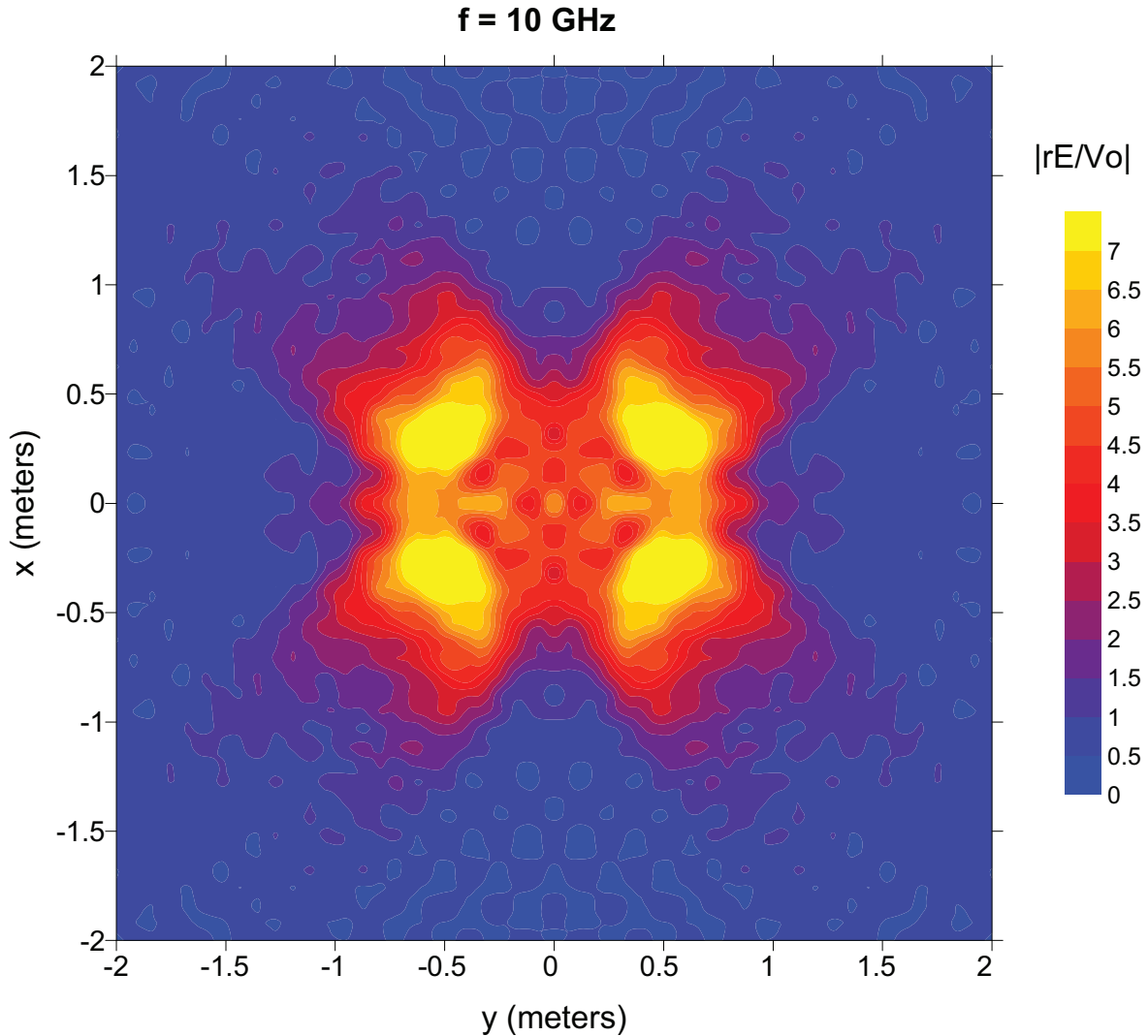
f = 10 GHz

Figure 29. Contour plots of the normalized near-field zE/V_o (at $z = 5$ m) for $f = 10$ GHz, showing the local field distribution.

It is also interesting to plot the radiated E-field in a spherical coordinate system, as opposed to Cartesian coordinates over the observation plane in Figure 21. Figure 30 illustrates a standard spherical coordinate system, with parameters r, θ and ϕ serving to describe the location of a field observation point. For this coordinate system, the principal E-field radiation pattern in the vertical plane (for $\phi = 90^o$ and θ variable) is plotted in Figure 31. In this figure, a family of curves representing the quantity $\log_{10}\left(rE(f)/V(f)\right)$ is plotted with the frequency varying from 100 MHz to 5 GHz.

Figure 32 presents a similar plot of the normalized radiation pattern in the horizontal plane (for $\phi = 0^o$ and θ variable).
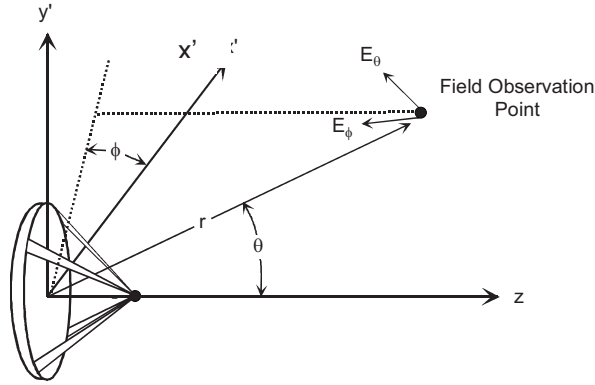
Figure 30. Coordinate system geometry for the far-field presentation of the E-field radiated from the IRA.
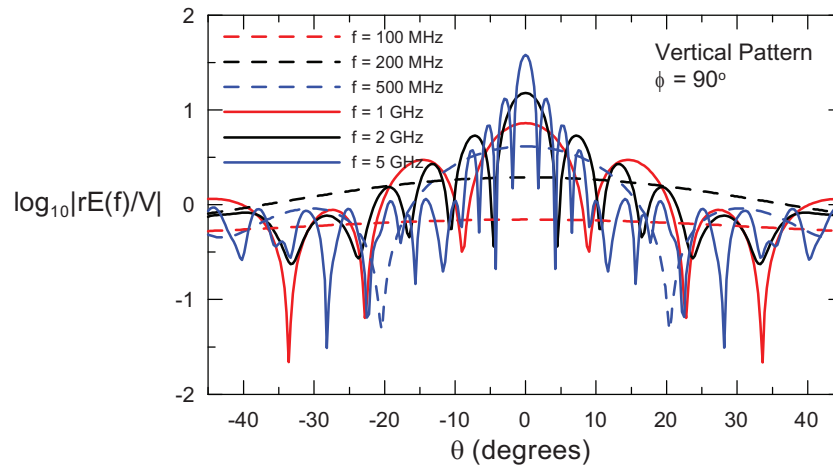

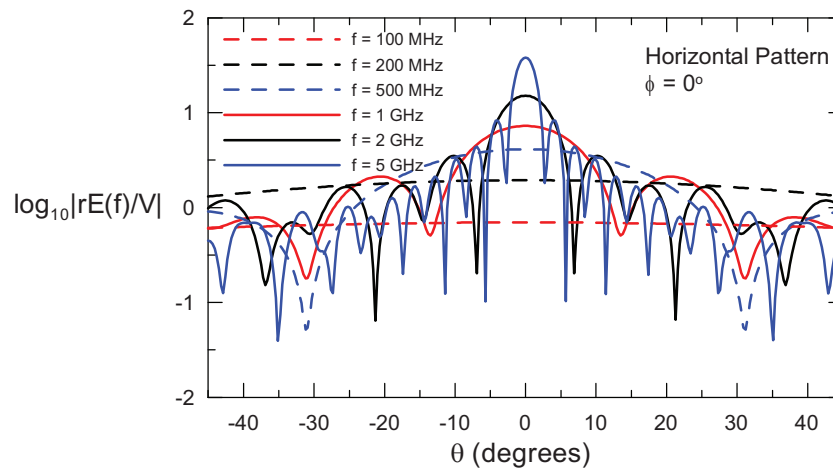**Figure 31. Plot of the wide-angle normalized radiation pattern of the SWIRA in the vertical plane.**

Figure 32. Plot of the wide-angle normalized radiation pattern of the SWIRA in the horizontal plane.

35

3.2 Vertically Polarized SWIRA Near the Earth

As noted in Section 2.5 the presence of an imperfectly conducting earth can modify the radiation behavior of an IRA. The SWIRAs are located as shown in Figure 13 with its center line about 1.5 meters over the earth. For this antenna excited in the vertical polarization mode, calculations of the transient boresight E-field at various ranges and a height $h_2 = 1.5$ m were made, and the results are presented in Figure 33. For these calculations, the earth parameters were $\sigma = 0.01$ S/m and $\varepsilon_r = 10$.

We note in the waveforms of Figure 33 the earth-reflected field is not very significant for observation locations close to the IRA. This is because the direct ray leaving the antenna is along the boresight direction, where it is very large in amplitude, while the earth-reflected ray leaves the antenna at a very large angle from the boresight direction, and the wave amplitude is much smaller. Moreover, for observation locations close to the antenna, the arrival time of the earth-reflected wave is significantly greater than that of the direct wave (see Figure 14) and the total E-field waveform is seen to have two distinct components. As the observation point recedes from the antenna, the angle ψ in Figure 13 passes through the Brewster angle and the reflected field is very small. (See the waveform for $z = 10$ m).

As the observation point continues to recede, the direct and reflected waves begin to overlap and cancel each other, with the result that the peak amplitude of the radiated transient E-field with the earth present becomes smaller than that radiated in free space.

It is useful to plot the earth-reflected and surface wave contribution to the total field by itself, as shown in Figure 34. Part a of this figure clearly shows the Brewster angle effect, which occurs at a range of approximately 10 meters. Here the green plot is nearly zero, and the polarity of the waveforms on either side of this range (5 and 20 meters) is seen to change.

Figure 18 has displayed the peak value of the radiated transient E-field for the SWIRA in free-space. Figure 35 is a re-plot of these data, together with the peak values for the E-field of the SWIRA operating in the presence of the lossy earth. As noted in this figure, as long as the observation point is within 100 meters of the antenna the peak field is simply given by the free-space value. At greater distances, however, the field falls off more rapidly than $1/r$, due to the cancellation of the direct and reflected waves.

The spectral responses of the transient fields of Figure 33 are presented in Figure 36. These responses are to be compared with those of Figure 25 for no earth present.
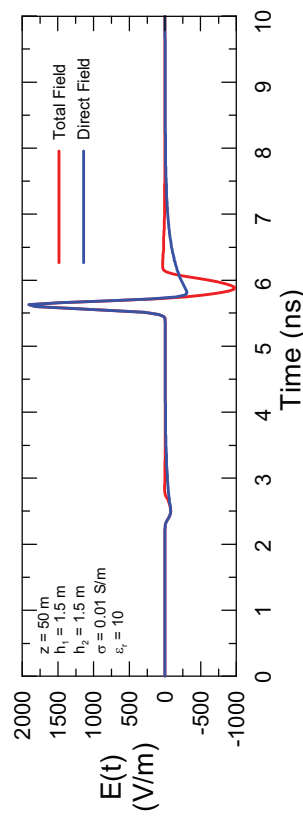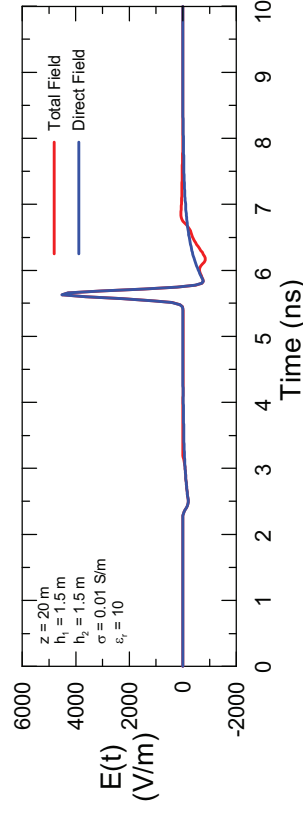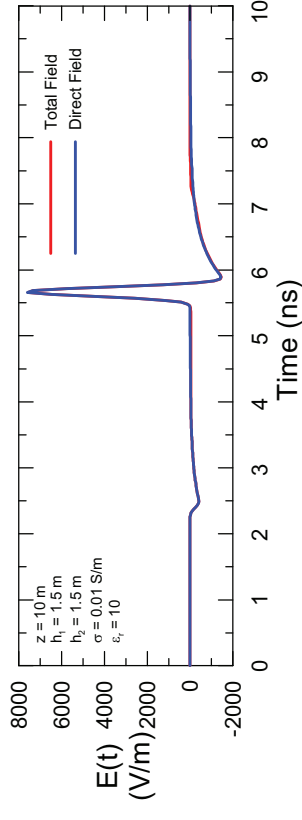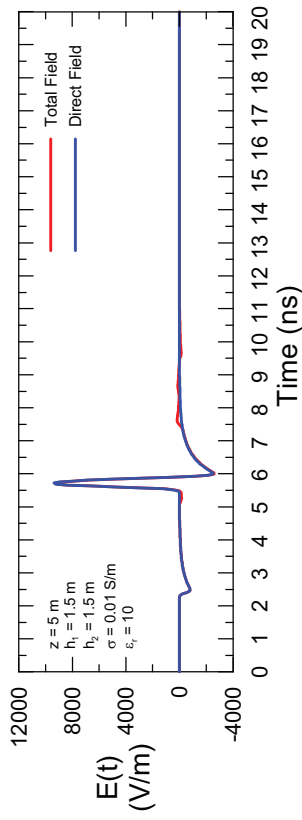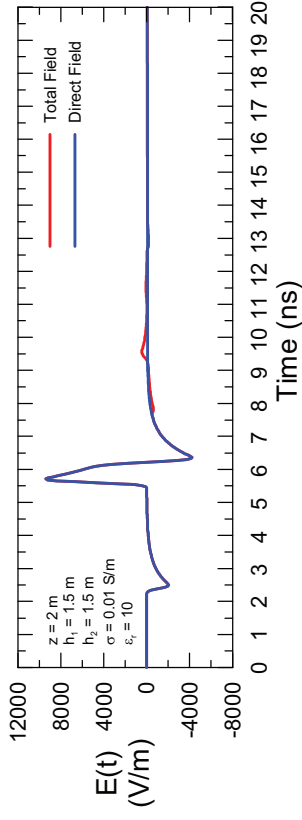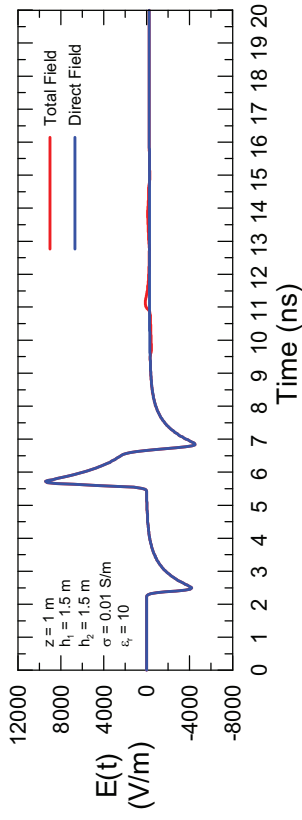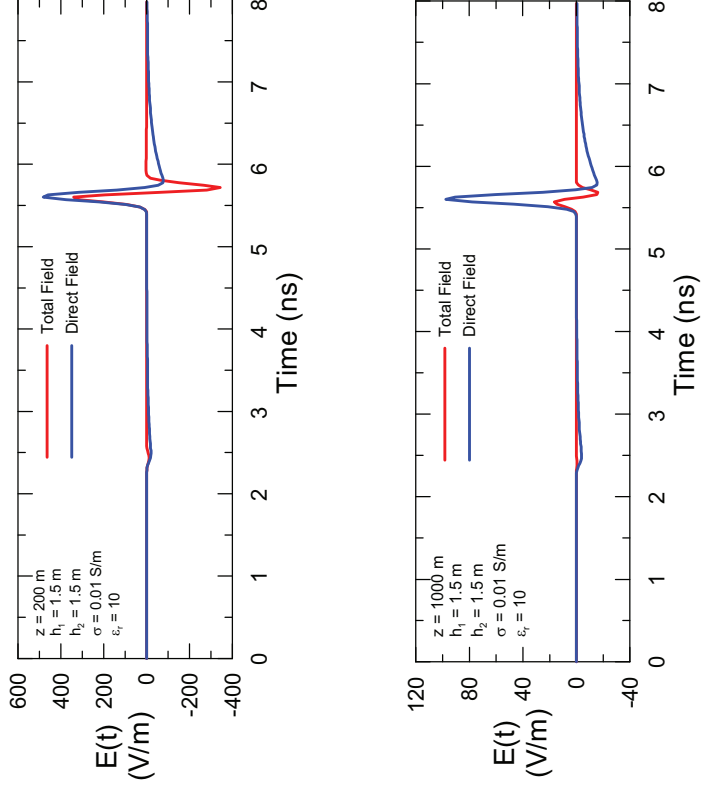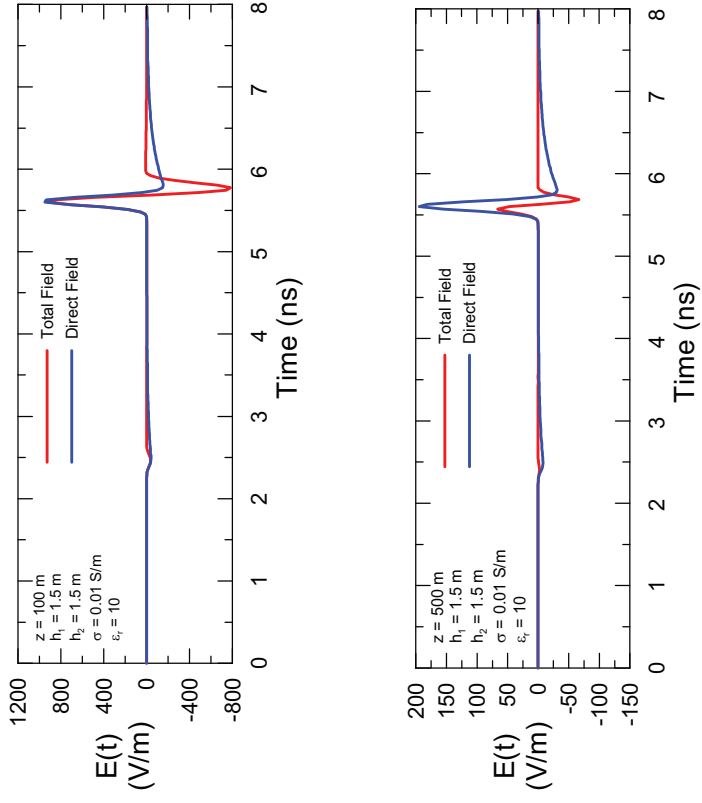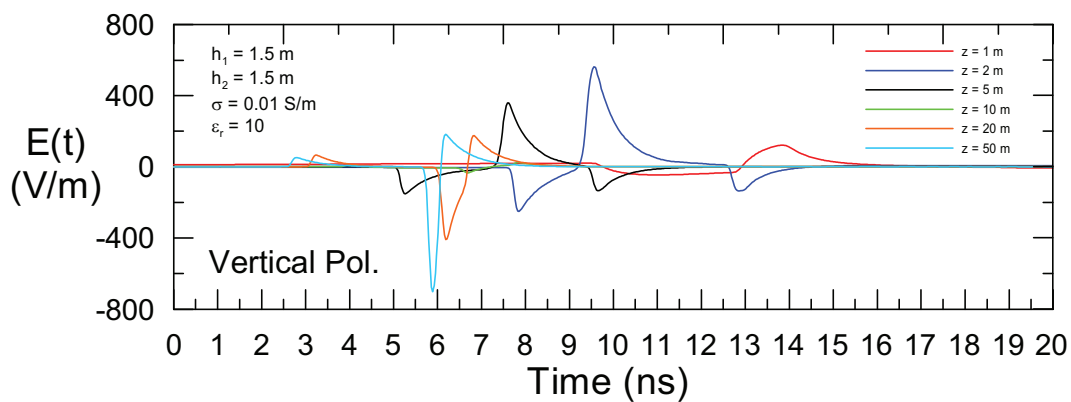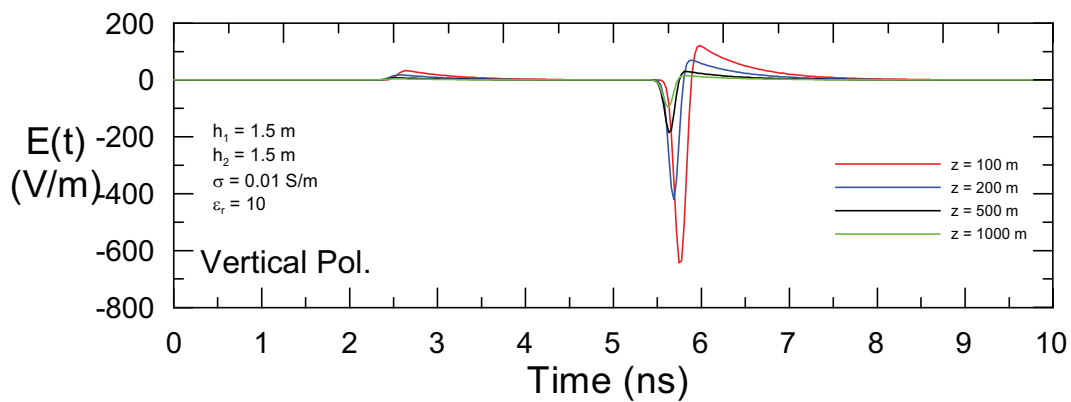
Figure 33. Plot of the on-axis vertically polarized E-field (E_y) for the SWIRA located **1.5 m** over a lossy earth with $\sigma = 0.01$ **S/me and $\varepsilon_r = 10$.**

38

a. Range from 1 to 50 m.

b. Range from 50 to 1000 m.

Figure 34.   Plots of the transient earth-reflected field from the SWIRA for different ranges, *z*, from the antenna with vertical polarization.
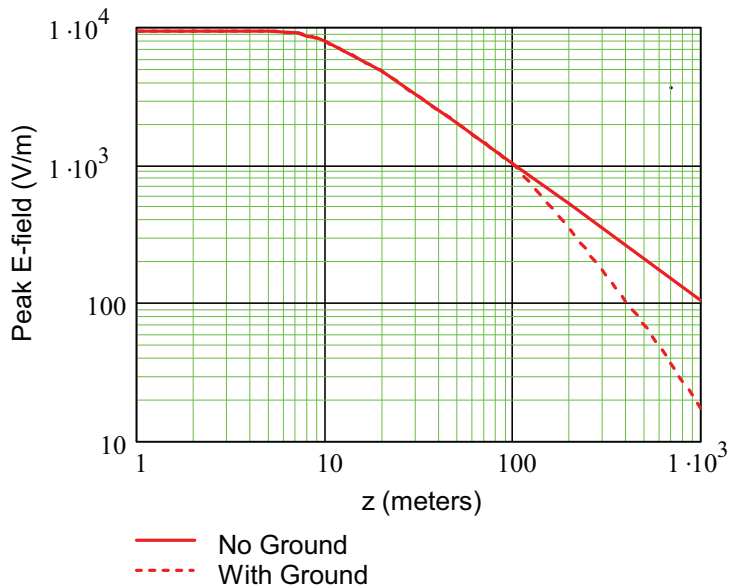
Figure 35. **Peak value of the on-axis E-field from the SWIRA as s function of range, with and without the ground present. (Vertical polarization).**
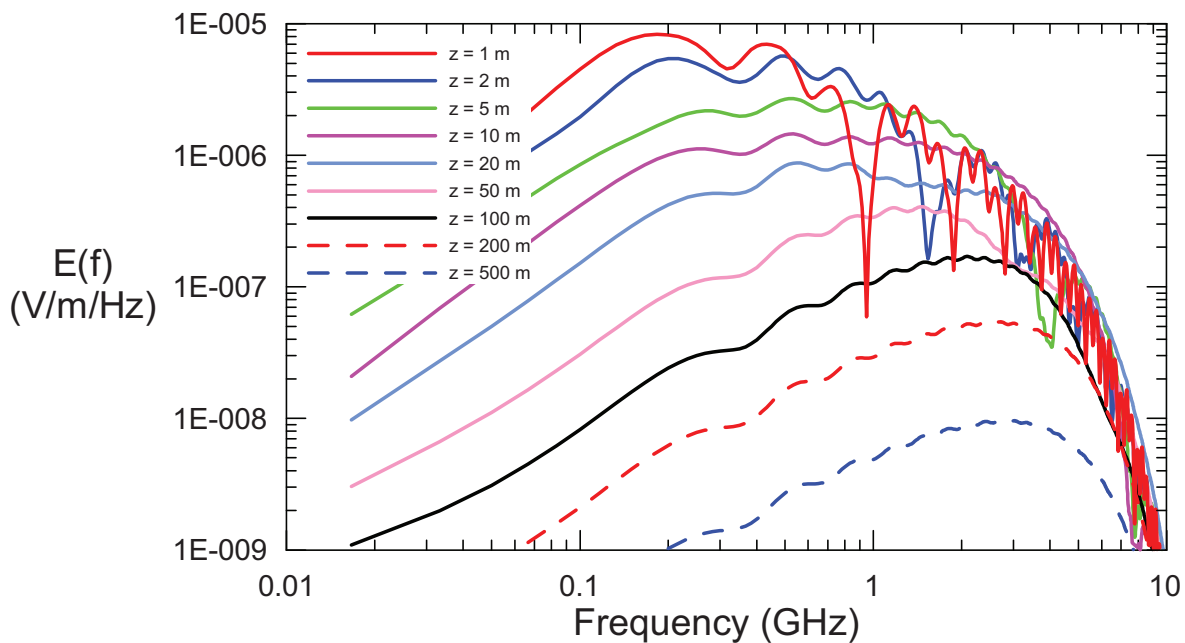

Figure 36. **Plot of the spectral magnitudes of the on-axis E-field for vertical polarization for the SWIRA located 1.5 m over a lossy earth with $\sigma = 0.01$ S/m and $\varepsilon_r = 10$.**
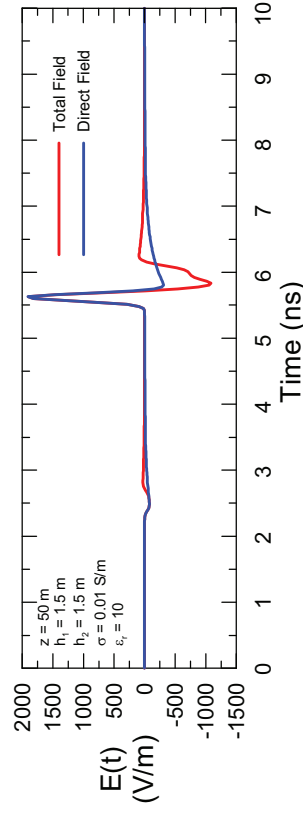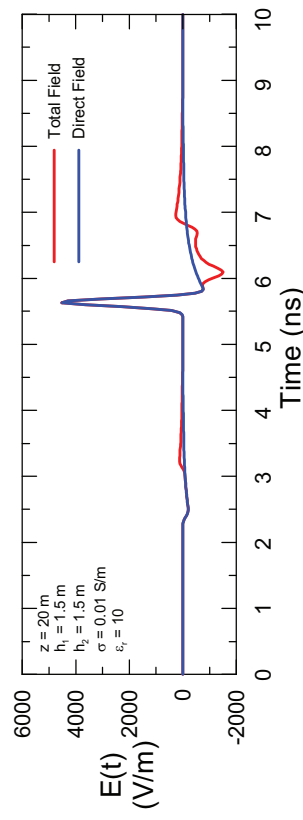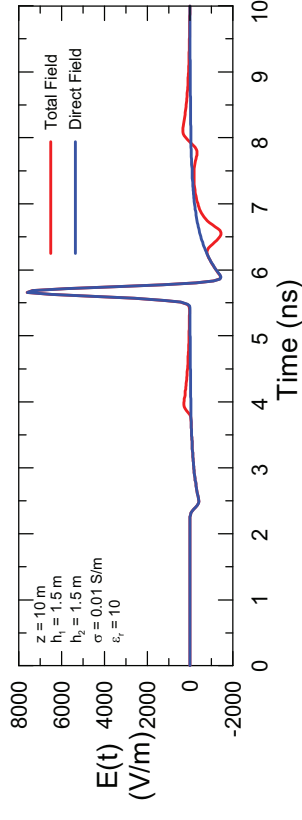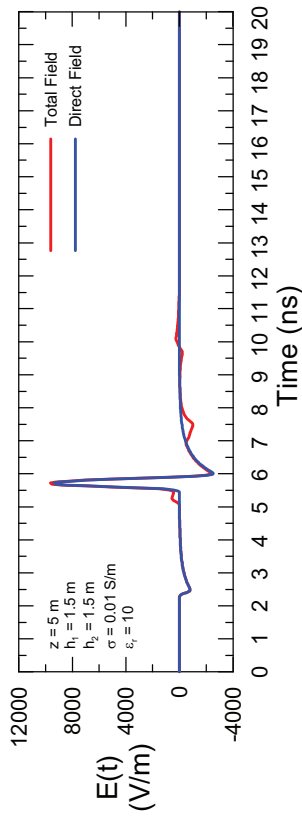
40

3.3 Horizontally Polarized SWIRA near the Earth

Calculations similar to those for the vertical polarization case also have been made for the horizontally polarized SWIRA. As noted in Section 2.5 the main difference lies in the use of the horizontal reflection coefficient.

Figure 37 provides plots of the on-axis horizontally polarized transient E-field (E_x) for this case. In examining these results, we note that there is no Brewster angle effect, where the earth-reflected wave becomes small. However, we note that at long ranges, the direct incident and earth-reflected fields still cancel and the resulting waveform is significantly smaller in amplitude than the direct, free-space field.

Figure 38 presents the transient earth-reflected and surface wave component of the field for different ranges. In this plot, it is clear that there is no Brewster angle effect.

Figure 39 presents the corresponding frequency domain spectral magnitude for the waveforms of Figure 37.

Top-left plot: z = 1 m, h₁ = 1.5 m, h₂ = 1.5 m, σ = 0.01 S/m, εᵣ = 10. E(t) (V/m) axis 12000 to -8000, Time (ns) 0–20. Legend: Total Field, Direct Field.

Top-right plot: z = 2 m, h₁ = 1.5 m, h₂ = 1.5 m, σ = 0.01 S/m, εᵣ = 10. E(t) (V/m) axis 12000 to -8000, Time (ns) 0–20. Legend: Total Field, Direct Field.

Middle-left plot: z = 5 m, h₁ = 1.5 m, h₂ = 1.5 m, σ = 0.01 S/m, εᵣ = 10. E(t) (V/m) axis 12000 to -4000, Time (ns) 0–20. Legend: Total Field, Direct Field.

Middle-right plot: z = 10 m, h₁ = 1.5 m, h₂ = 1.5 m, σ = 0.01 S/m, εᵣ = 10. E(t) (V/m) axis 8000 to -2000, Time (ns) 0–10. Legend: Total Field, Direct Field.

Bottom-left plot: z = 20 m, h₁ = 1.5 m, h₂ = 1.5 m, σ = 0.01 S/m, εᵣ = 10. E(t) (V/m) axis 6000 to -2000, Time (ns) 0–10. Legend: Total Field, Direct Field.

Bottom-right plot: z = 50 m, h₁ = 1.5 m, h₂ = 1.5 m, σ = 0.01 S/m, εᵣ = 10. E(t) (V/m) axis 2000 to -1500, Time (ns) 0–10. Legend: Total Field, Direct Field.
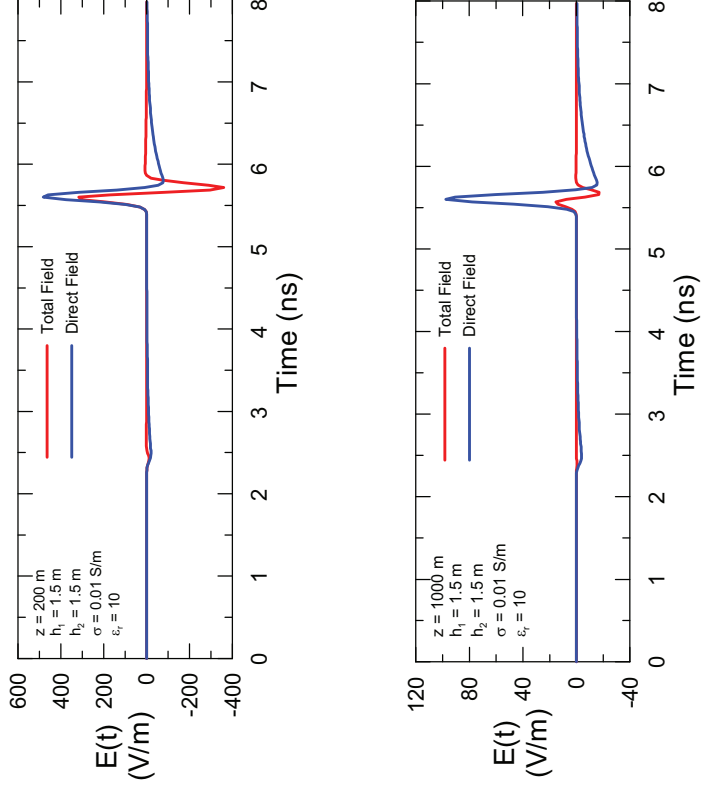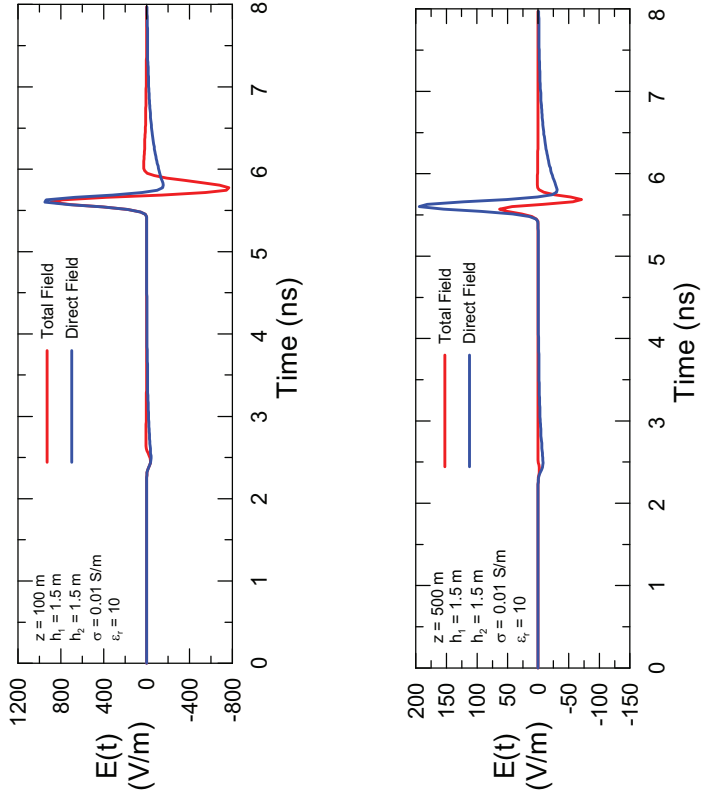
42
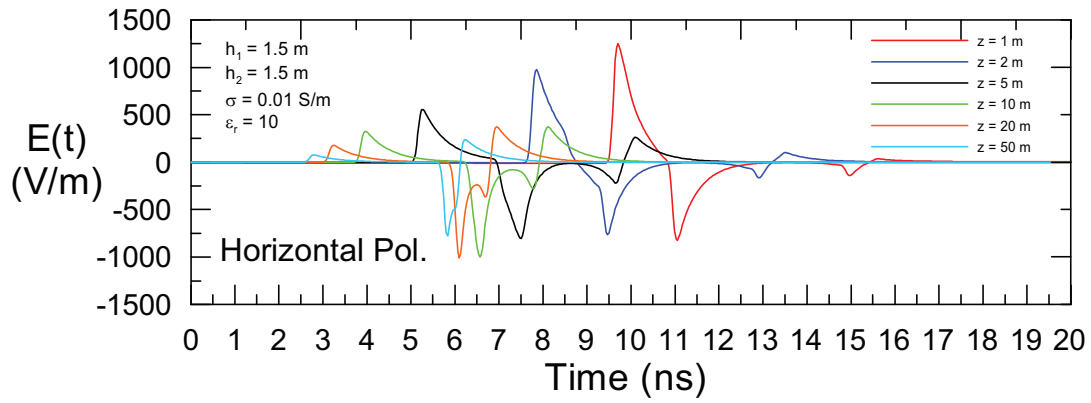
Figure 37. Plot of the on-axis horizontally polarized E-field (E_x) for the SWIRA located 1.5 m over a lossy earth with $\sigma = 0.01$ S/m and $\varepsilon_r = 10$.

a. Range from 1 to 50 m.
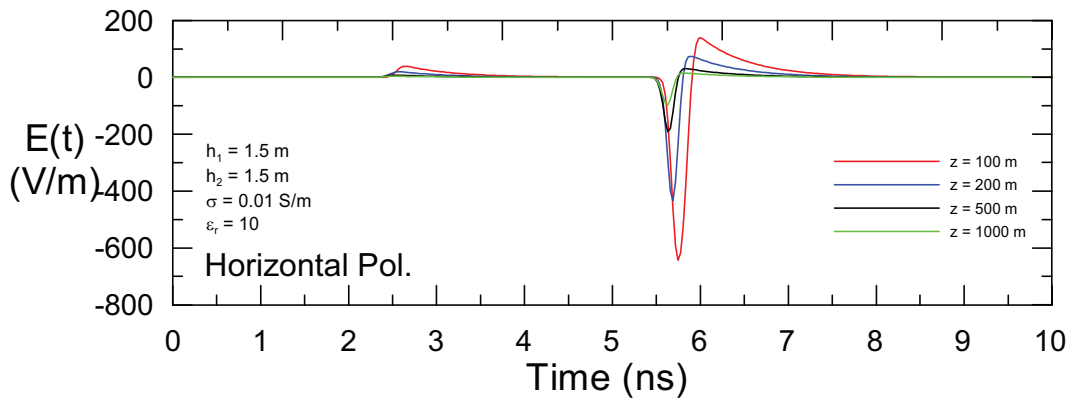
b. Range from 50 to 1000 m.

Figure 38.   Plots of the transient earth-reflected field from the SWIRA for different ranges, *z*, from the antenna with horizontal polarization.

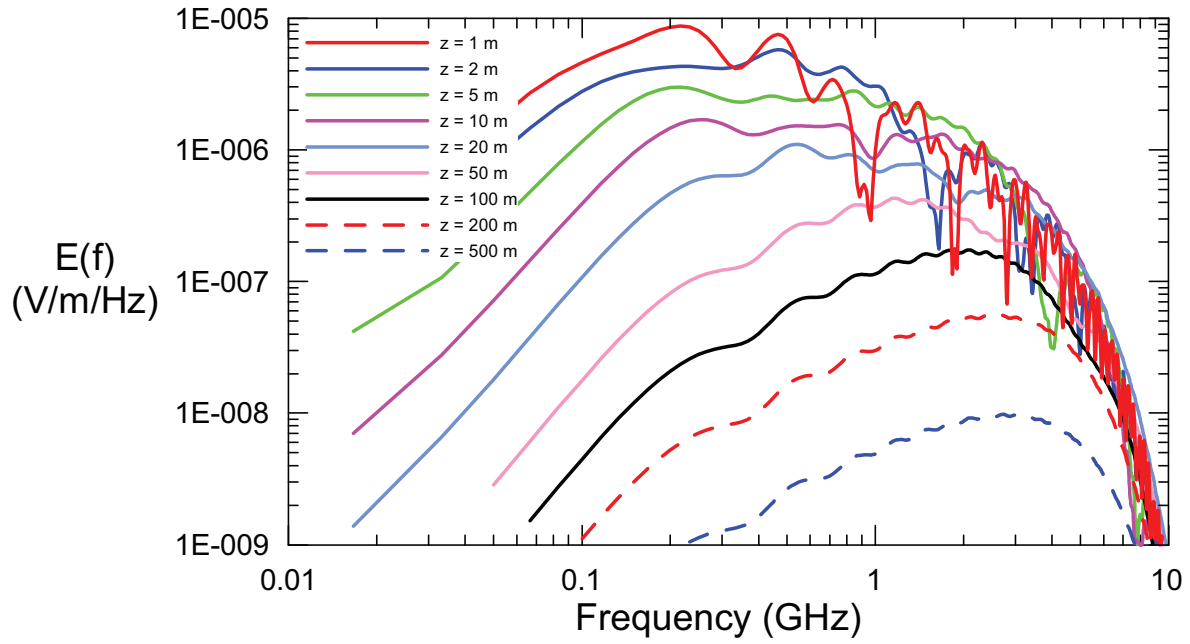**Figure 39.** Plot of the spectral magnitudes of the on-axis E-field for horizontal polarization for the SWIRA located 1.5 m over a lossy earth with $\sigma = 0.01$ S/m and $\varepsilon_r = 10$.

4. Summary

This note has summarized a computational model for computing the radiated E-field from the Swiss impulse radiating antenna (SWIRA). The model is based on integrations over equivalent magnetic current sources located in the antenna aperture, and over the electrical currents flowing on the transmission line feed arms. These integrations provide the E-field at a distant observation point in the frequency domain, and with knowledge of the pulser waveform exciting the antenna, the transient E-field can be synthesized using Fourier transform techniques.

Using this model a parametric study of the antenna's E-field distribution has been conducted. Both transient and frequency domain results have been obtained for both the on-axis (boresight) and off-axis locations of the observation points.

From these calculations, a number of important observations about the antenna behavior have been made. These are summarized as follows:

1. The aperture/feed-line integration method compares almost exactly with the analytical results of ref.[11] for observation points in the boresight direction. However, unlike the method of [11], the present analysis is valid for observation points far away from boresight.

2. The radiated transient field from the antenna contains two basic components: a relatively low level pulse at the start of the waveform, which is referred to as the "prepulse", and a later impulse-like spike, which is the desired radiated field from the SWIRA.

3. For observation locations close to the antenna, the peak value of the transient E-field is seen to be approximately 10 kV/m and this remains nearly constant over the range $1 \leq z \leq 10$ m. This is the near-field region of the antenna.

4. For observation points in the range $10 \leq z \leq 40$ m, there is a transition behavior of the radiated E-field, changing from a constant field to one which falls off a little slower than 1/z. This is the intermediate region.

5. For observation locations greater than about 40 m from the antenna, we note that the impulse-like peak of the transient radiated field decreases in amplitude by a factor 1/z. This behavior is typical of a far-field response of the antenna.

6. Another measure of the far-field of the SWIRA is given by Eq.(1), which puts the far-field as starting at $z \approx 38$ m.

7. In the frequency domain, the spectral magnitude of the radiated E-field (see Figure 25) is more or less constant from about 200 MHz to 2 GHz. Outside this range of frequencies, the spectral content decreases roughly proportionally to frequency. At low frequencies, this spectral fall-off is due to the fundamental limitations of the aperture radiation, and at high frequencies, the fall-off is due the limited spectral content of the excitation pulser waveform.

8. Although the model for the IRA shows stable results for frequencies up to and exceeding 10 GHz (see Figure 26), there will be a practical limit of the actual operation of the antenna of about several GHz. This is due to inevitable asymmetries associated with the construction of the feed cables and structural elements of the antenna.

9. In examining the behavior of the transient E-field peak value for observation points off of the boresight direction (see Figure 24) we note that close to the antenna($z < 20$ m) the region of peak value is relatively small – a circular region with diameter of less than about 1 meter. Farther away, this region of peak field grows in size. However, the angle subtended by this beam tends to tighten as the distance from the antenna increases.

10. When the SWIRA is operated next to a lossy earth, the waveform is modified by an earth-reflected component. For the SWIRA height of 1.5 m over the earth, and for an observation point at the same height, it is noted (see Figure 33) that the peak radiated E-field is not affected by the earth as long as the observation distance is less than or equal to about 100 m. Thus, for distances $z \leq 100$ m, the earth effects on the peak transient amplitude can be neglected.

11. Using Eqs.(12) and (13) for these antenna and observation heights of 1.5 meters, the earth reflected field is seen to arrive at the observation point at $z = 100$ m retarded in time by about 1.7 ps. Using this time as an indication of when the peak field amplitude will be affected by the earth, Eqs.(12) and (13) can be used with other SWIRA and/or observation heights to compute the range at which earth effects are important.

12. As noted in Figure 35, the peak transient E-field falls off more rapidly than 1/z when the earth effects are important (e.g., for $z > 100$ m for the 1.5 meter heights of the SWIRA and observation point.)

5. References

1.   D. V. Giri, A. Kaelin and B. Reusser, "Design, Fabrication and Testing of a Prototype Impulse Radiating Antenna", NEMP Laboratory Memo, 1 July 1997.

2.   I. D. Smith, D. W. Morton, D. V. Giri, H. Lackner, C. E. Baum, J. R. Marek, " Design, Fabrication and Testing of a Paraboloidal Reflector Antenna and Pulser System for Impulse-Like Waveforms", *Proceedings of the Tenth IEEE International Pulsed Power Conference*, Albuquerque, NM, July 3-6, 1995, Vol. 1, pp 56-64. Also in *IEEE Trans Plasma Science*, April 1997, pp 318-326.

3.   C. E. Baum, "Radiation of Impulse-Like Transient Fields", *Sensor and Simulation Note 321*, 25 November 1989.

4.   F. M. Tesche and D. V. Giri, "High-Power Electromagnetic (HPEM) Testing of Swiss Civil Defense Facilities", Volume I – IV, Report for Contract 4500300423 from the Swiss Defense Procurement Agency, Department of Defense, Civil Protection and Sports, September 19, 2000.

5.   F. M. Tesche and P. F. Bertholet, "Test Report for 2003 Civil Defense Testing in Gurmels", Prepared for FOCP Contract No. 350000560, Berne, Switzerland, November 26, 2003.

6.   D. V. Giri, "Upgrading of the Swiss Impulse Radiating Antenna (SWIRA) and VEPES Upgrade Schedule", Final report submitted to NEMP Laboratory, armasuisse, Spiez 3700, Switzerland, December 2004.

7.   http://www.fidtechnology.com/

8.   E. G. Farr, "Development of a Reflector IRA and a Solid Dielectric Lens IRA", *Sensor and Simulation Note 396*, April 1996.

9.   C. E. Baum, "Configurations of TEM Feed for an IRA", *Sensor and Simulation Note 327*, 27 April 1991.

10.   D. V. Giri, . M. Lehr, W. D. Prather, C. E. Baum, and R. J. Torres, "Intermediate and Far Fields of a Reflector Antenna Energized by a Hydrogen Spark-Gap Switched Pulser", *IEEE Trans. Plasma Science*, Oct. 2000.

11.   Oleg V. Mikheev, et. al, "New Method for Calculating Pulse Radiation from an Antenna with a Reflector", *IEEE Trans. EMC*, February 1997.

12.   F. M. Tesche, et. al., *EMC Analysis Methods and Computational Models*, John Wiley and Sons, New York, 1997.

13. C. Balanis *Advances in Engineering Electromagnetics*, John Wiley & Sons, New York, 1989.

14. E. G. Farr, "Development of a Reflector IRA and a Solid Dielectric Lens IRA", *Sensor and Simulation Note 396*, April 1996.

15. E. G. Farr and C. E. Baum, "Prepulse Associated with the TEM Feed of an Impulse Radiating Antenna", *Sensor and Simulation Note 337*, March 1992.

16. F. M. Tesche, "Analysis of Swiss Civil Defense Test Data", Report prepared for Task 1, FOCP Contract No. 350000174, "Civil Defense Test and Analysis Support", Defense Procurement Agency of the Federal Department of Defense, Civil Protection and Sports, Sept. 19, 2001.

17. D. J. Angelakos and T. E. Everhart, *Microwave Communications*, McGraw-Hill, New York, 1968.

18. E. C. Jordan and K. G. Balmain, *Electromagnetic Waves and Radiating Systems*, Prentice-Hall, 1968, Englewood Cliffs, NJ.

19. F. M. Tesche, T. C. Mo and R. W. Shoup, "Determination of the Electromagnetic Fields Radiated from the ARES EMP Simulator", *IEEE Trans. EMC*, Vol. 36, No. 4, November 1994.

20, D. V. Giri, *High-Power Electromagnetic Radiators: Nonlethal Weapons and Other Applications*, Harvard University Press, November 2004.

Appendix A

Validation of the Aperture/Feed Line Integration Model

1. Introduction

Reference [1] has developed an analytical expression for the near- and far-field transient E-field produced by an IRA fed by a two-arm feed structure, similar to that shown in Figure 6 of this paper. This analysis has been modified slightly by Giri to permit the analysis of the on-axis field radiated by a four-arm SWIRA, as shown in Figure A1.

In this appendix, these analytical expression will be used to compute transient and spectral responses of the on-axis E-field from the SWIRA having a diameter $D = 1.8$ m and focal length $F = 0.482$ m. The resulting fields will be compared with those computed by the aperture/feed-arm integration method used in this report.
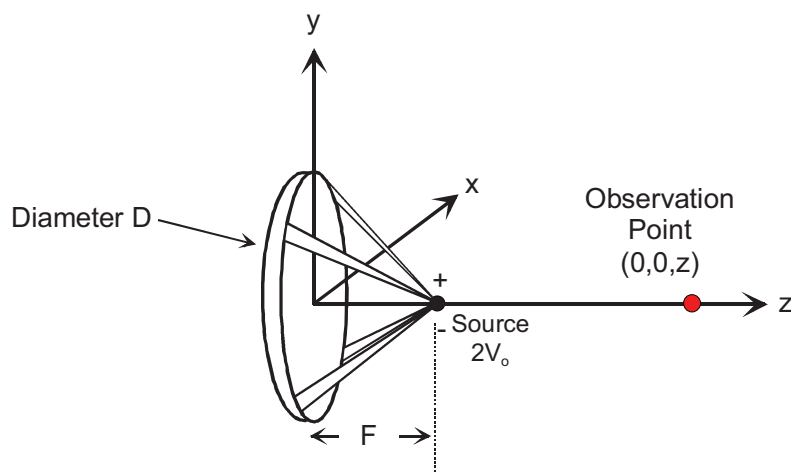

Figure A1. On-axis E-field responses for different values of distance z.

2. Comparison of Transient Responses

For the SWIRA shown in Figure A1, the transient responses of the on-axis E-field have been reported in Figure 17 of the note. These responses are reproduced below as Figure A2. Using the model of ref.[1], the resulting transient E-fields are presented in Figure A3. In comparing the results from these two analysis methods, we note that the agreement between the two is excellent.

---

[1]. Oleg V. Mikheev, et. al, "New Method for Calculating Pulse Radiation from an Antenna with a Reflector", *IEEE Trans. EMC*, February 1997.
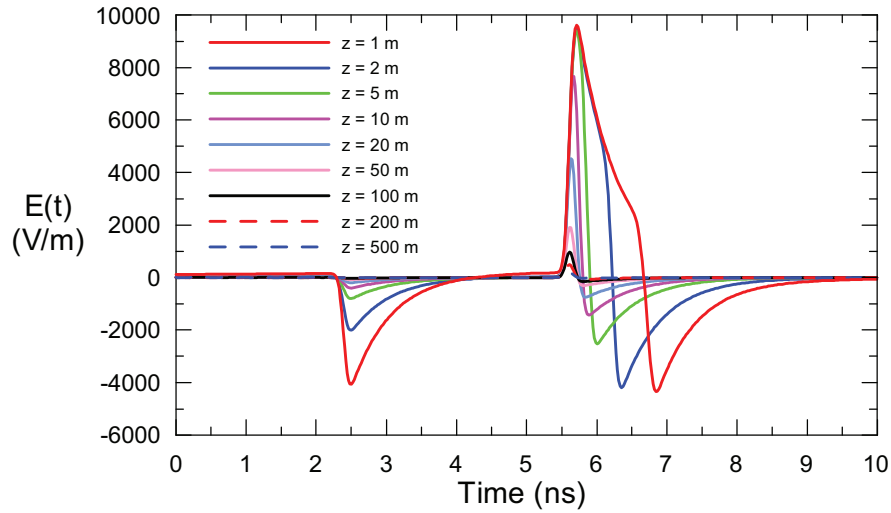
Figure A2.   Principal on-axis transient E-field produced by the SWIRA for different ranges *z*, as presented in Figure 17 of the report. (Computed using the aperture/feed-arm integration method.)
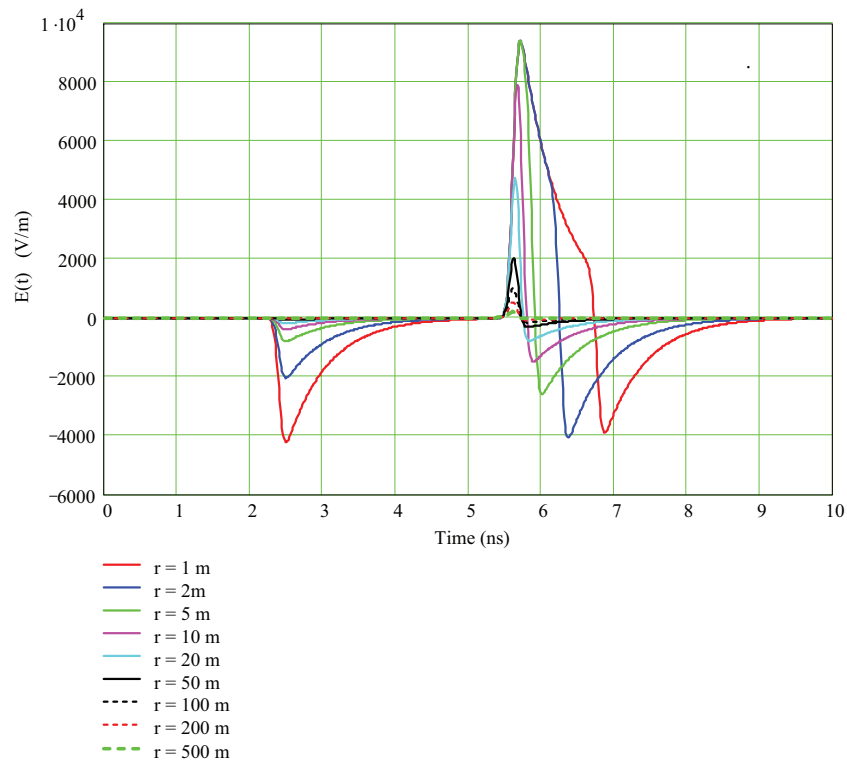

Figure A3.   The same E-field waveforms as in Figure A2, computed using the method of ref.[1].

51

3. Comparison of Spectral Responses

Similar comparisons of the spectral responses for the SWIRA have also been made. Figures A4 and A5 compare the E-field spectral magnitudes for the different observation locations, and Figures A6 and A7 compare the normalized E-field spectral magnitudes $(zE(\omega)/V(\omega))$. As in the case of the transient responses, the agreement between the two analysis methods is excellent.
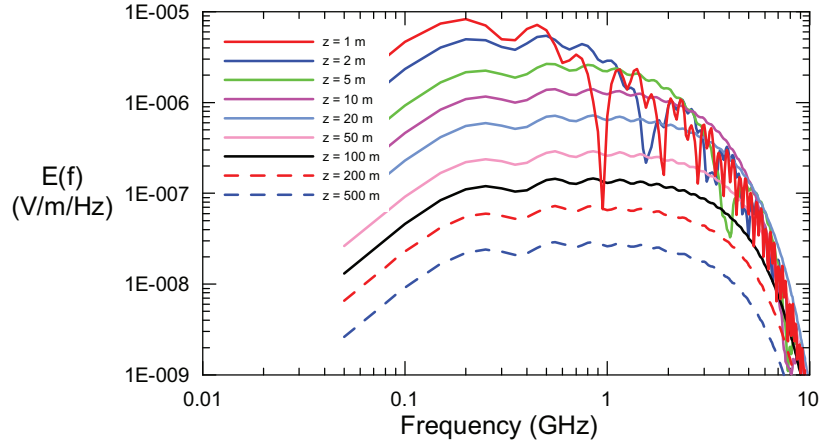

Figure A4. Plot of the spectral magnitude of the on-axis E-field of Figure A2 for different ranges, *z*. as provided by Figure 24 of the report. (Computed using the aperture/feed-arm integration method.)
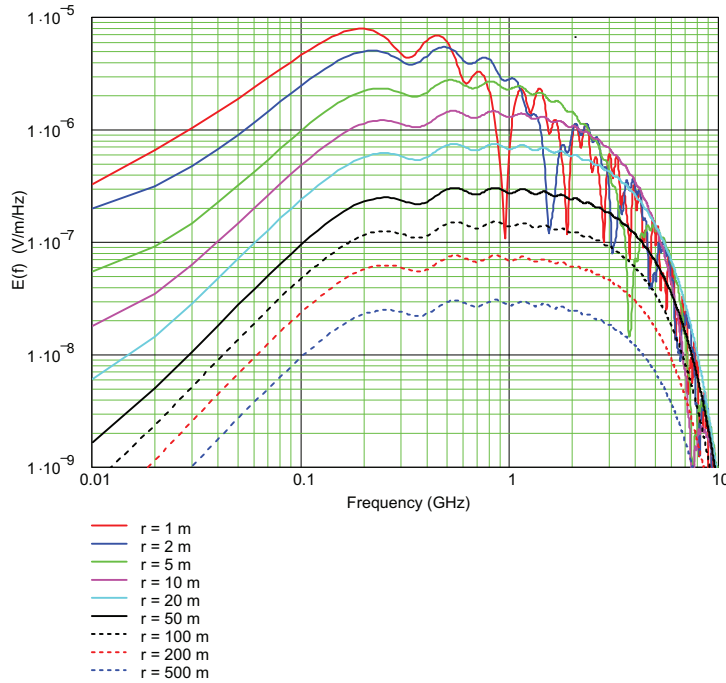

Figure A5. The same E-field spectral magnitude as in Figure A4, computed using the method of ref.[1].
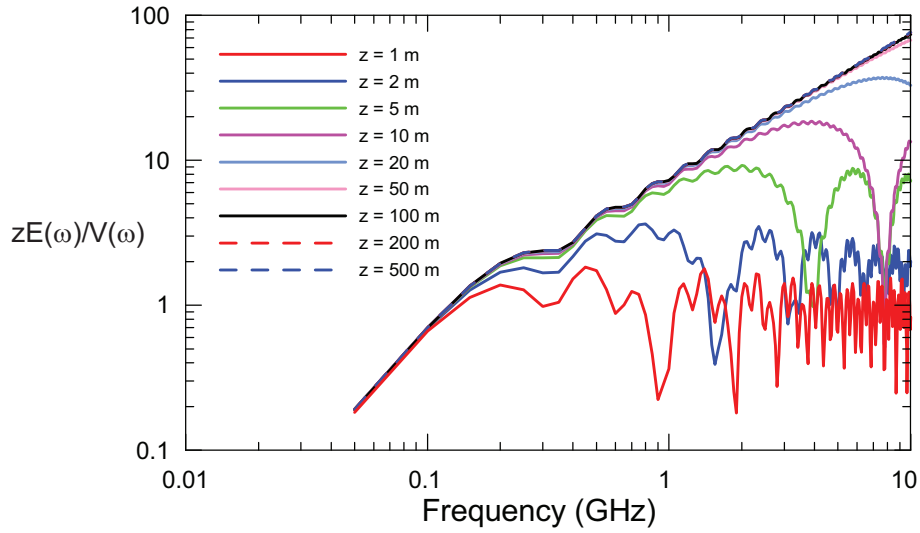
Figure A6. Plot of the normalized on-axis E-field transfer function magnitude ($zE(\omega)/V(\omega)$) for different ranges z as provided by Figure 25 of the report. (Computed using the aperture/feed-arm integration method.)
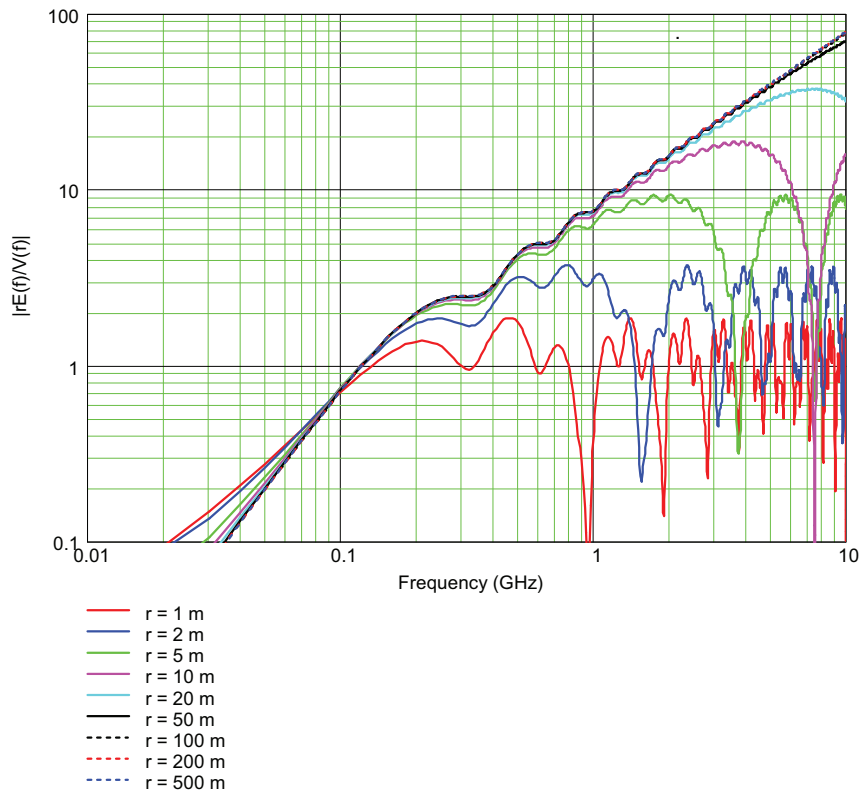

Figure A7. The same E-field spectral magnitude as in Figure A6, computed using the method of ref.[1].